Simulation of the Fountain Flow Effect by Means of the Radial Functions Method (RFM)

Daniel Ramírez C.

Submitted in partial fulfillment
of the requirements for the degree of
Magister of Science

EAFIT University
College of Engineering
Department of Production
Medellín
2011

-

Dedicada a mi padre.

Contents

List of Figures

List of Tables

Chapter 1

Introduction

Injection molding is an ideal process for the mass production of parts with complex shapes. It is one of the most important, common, and economically relevant polymer processes: more than half of all polymer processing equipment is for injection molding and approximately one third of all the thermoplastic material manufacturing is done by using injection molding[32]. The process, which is cyclic in nature, can be divided into the following steps[26]:

- Melting of plastic
- Injection of the melt into the mold cavity
- Cooling of the mold
- Removal of the article

The material is molten and mixed in the plasticating unit. Then, it is injected using high pressure into the mold. When the part has cooled and solidified, it is removed from the mold. The whole injection process with its different phases can be visualized in Figure 1.1.

In Figure 1.2, a reciprocating injection machine (which is the most common type of injection machine currently used) is shown with its main parts.

For the sake of study and analysis, the flow inside the mold cavity can be divided into three characteristic regions according to Figure 1.3:

- The gate region
- The fully developed region

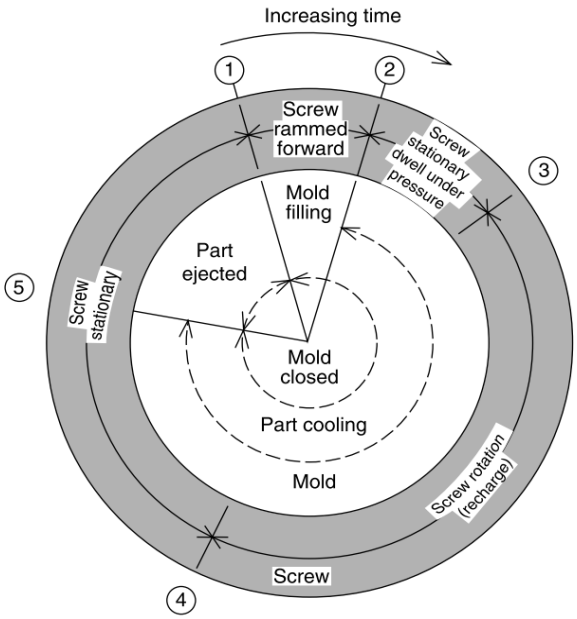

Figure 1.1: Injection cycle phases[39].

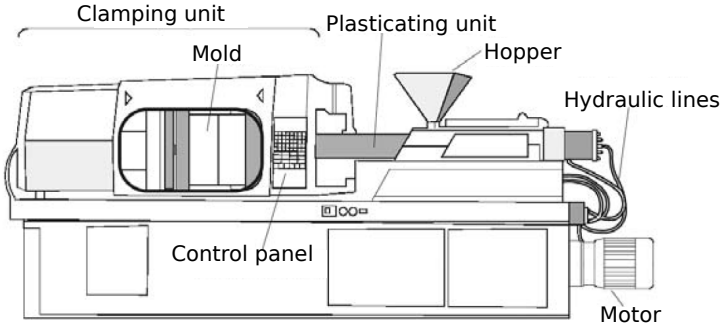

Figure 1.2: Injection molding machine (schematics)[30].

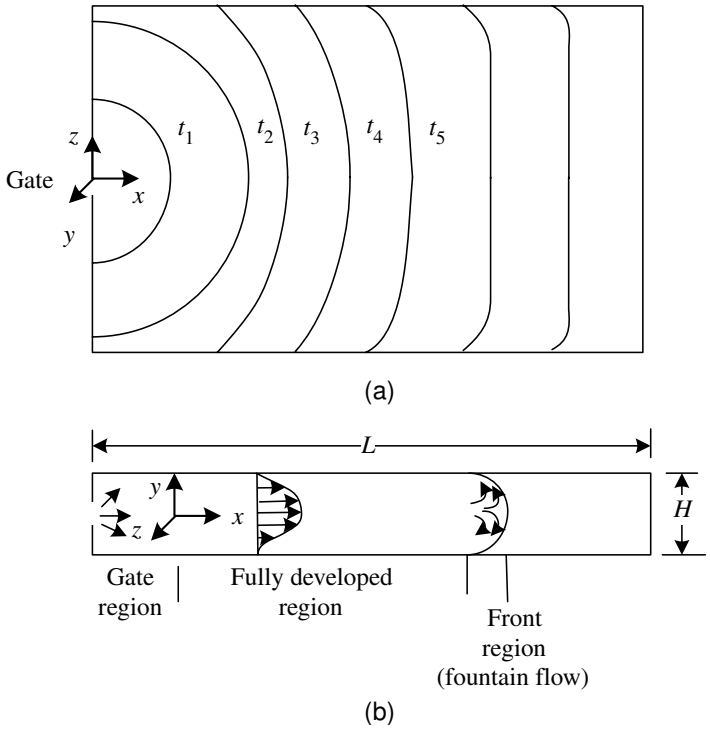

Figure 1.3: Mold filling zones [39].

- The front region (fountain flow region)

In the close neighborhood of the flow front, the material spills from the center of the channel to walls. This phenomenon known as the *fountain flow effect* (a term coined by Rose [35]) is the only way to fill the regions near the walls where a non-slip velocity condition exists. The characteristic velocity patterns of the fountain flow effect can be seen in Figure 1.4. Figure 1.4(a) corresponds to a stationary reference frame, whereas in Figure 1.4(b) the reference system moves with the average velocity of the flow.

The fountain flow effect affects the orientation of the macromolecules and, therefore, the mechanical and optical properties of injection molded parts [2]. In the case of reinforced materials, it affects the distribution and orientation of fibers [31, 39, 2]. Besides, since weld lines occur where two flow fronts impinge, the study of fountain flow effect is important to understand the

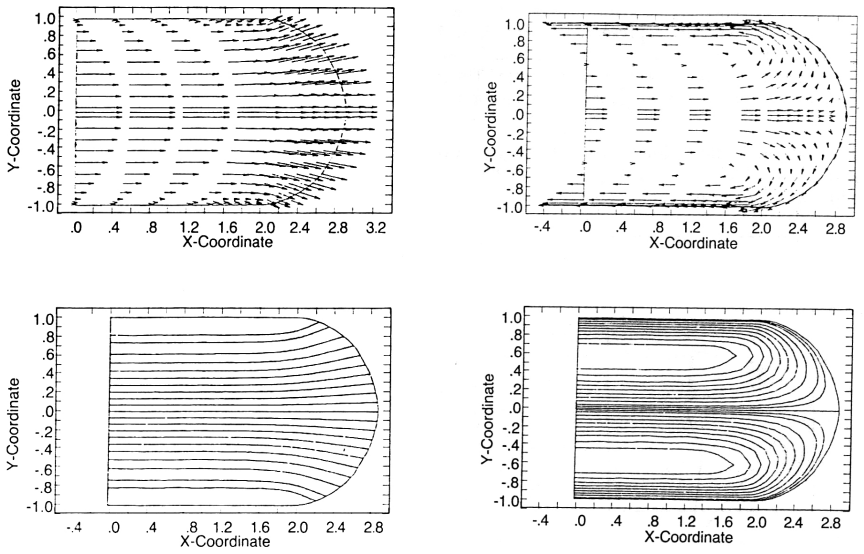

(a) Reference system fixed to the mold walls.

(b) Reference system that moves with the average velocity of the flow.

Figure 1.4: Streamlines and vector plots of the velocity fields associated to the fountain flow effect [31].

micromorphology of these regions.

Furthermore, in the fountain flow region, material with a high temperature moves from the center of the channel towards the walls of the mold. Therefore, the fountain flow effect could have an important influence on the temperature distribution during the filling. Since the existing commercial simulation software for injection molding uses the Hele-Shaw approximation, neglecting the velocities in the thickness direction, or rather coarse 3D solutions that do not capture well the details of the front flow kinematics, the influence of the fountain flow on the development of the temperature field during filling has not been studied in detail.

In order to simulate all the important phenomena that occur in an injection molding process, fully tridimensional simulations must be developed. Given the complexity and computational costs associated to that kind of simulations, most commercial injection molding simulation softwares are not based in true 3D schemes but in the Hele-Shaw approximation. This approach is effective in predicting important variables such as the pressure distribution, clamping force, position the weld lines and air entrapments. However, since the velocity in the thickness direction is ignored, the Hele-Shaw approach does not account for the fountain flow effect and its implications.

Although orientation can be used in the extrusion process to improve the mechanical performance of the product, in an injection molding process it is usually considered detrimental [41]. Differences in shrinkage are related to the changes in the orientation of the macromolecules. Figure 1.5 shows the shrinkage distribution for a polystyrene part. The fountain flow effect results in an elongational flow at the front that affects the orientation of the macromolecules (Figure 1.6). Besides, the material that forms the skin of the part travels from the center and is deposited in the walls during the mold filling (also by means of the fountain flow effect)[39]. These two phenomena explain the presence of a maximum in the shrinkage at the wall. In Figure 1.5, a secondary maximum can be noticed. This secondary maximum in the shrinkage distribution can be explained by the presence of a maximum in the shear rate near the wall in the developed flow region (Figure 1.7). Since this shear tends to align the macromolecules in the direction of the flow, the secondary maximum is absent when the shrinkage in the thickness direction is considered.

The purpose of this work is to simulate the fountain flow effect using a meshless technique (RFM) and, therefore, to explore the possibilities that the method offers for free surface problems. To the knowledge of the author, the

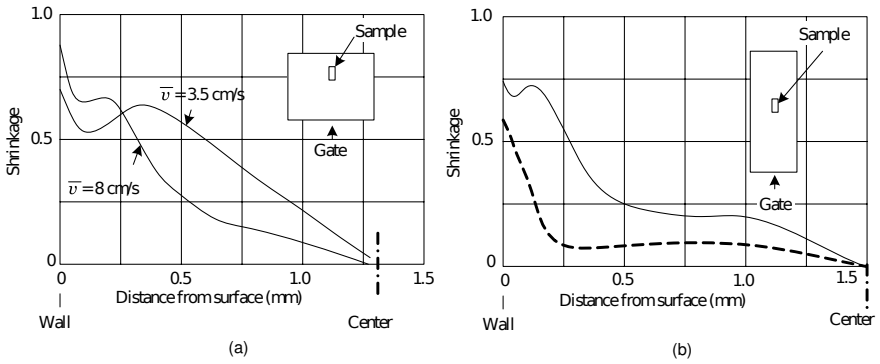

Figure 1.5: Shrinkage distribution for injection molded amorphous PS parts. (a) Shrinkage in the longitudinal direction for different injection rates. (b) Shrinkage in the longitudinal direction (solid lines) and shrinkage in the transversal direction (broken lines)[39].

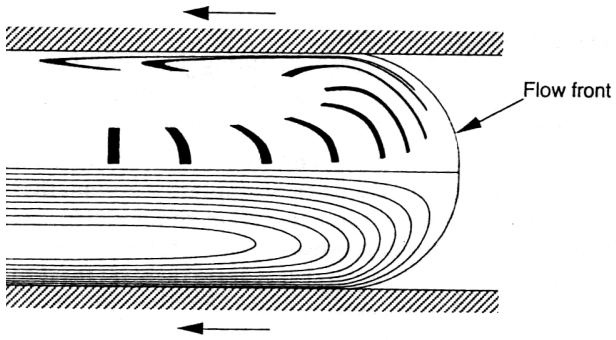

Figure 1.6: Deformation history of a fluid element as seen in a reference frame that moves with the average flow velocity[31].

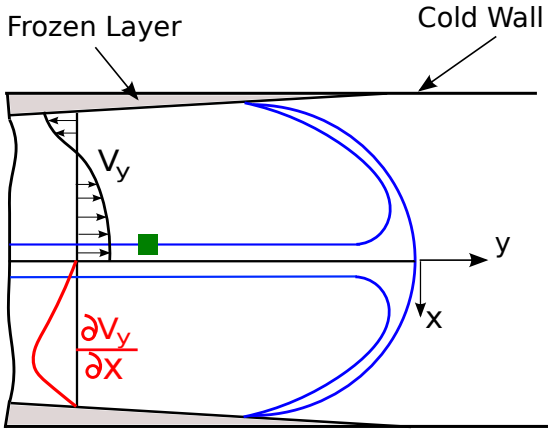

Figure 1.7: Schematic representation of the flow patterns in an advancing front between two plates. Notice the maximum in the shear rate upstream, in the developed flow region[2].

fountain flow effect has not been simulated in the past by means of meshless techniques.

In this thesis, a steady state was assumed for all simulations. This assumption is common in the literature and can be found for instance in [28, 27]. It originates from the consideration of a reference system that moves with the average velocity of the flow. For the flow in a slit, a power law model model with n varying between 0.6 and 1.1 was used to describe the variation of the viscosity with the shear rate. Another case considered in this thesis is the fountain flow of a Newtonian fluid in an axisymmetric tube including the force of gravity.

The organization of the thesis is as follows:

Chapter 2 presents a brief overview of the literature corresponding to the simulation of the fountain flow effect. In Chapter 3, the Radial Functions Method is presented using the solution of the Poisson equation as an example. Chapter 4 deals with the implementation of the method to simulate the fountain flow effect; this entails the representation of the motion and continuity equations, and the appropriate boundary conditions (including the free boundary) in terms of Radial Basis Functions. The thesis ends with chapters corresponding to the conclusions derived from the simulations and a presentation of possible lines of research for future work.

Chapter 2

Overview of the Literature

The first simulations of the fountain flow effect were developed during the 80's by different authors [24, 22, 7, 3, 25, 23].

Mavridis [24] *et al.* were the first to predict the position of the flow front for Newtonian, power-law and Carreau fluids using a numerical scheme that was based on FEM to solve the motion and continuity equations and on an iterative scheme to find the front shape. Their results show that the kinematics of the flow are basically the same for those fluids, having very similar streamlines patterns. In order to alleviate the problems related to the stress singularity, a slip condition was introduced in the contact point between the wall and the front. Besides, they found that for a power law fluid with $n = 0.5$ the front flow has a shape that is very close to a semicircle (Figure 2.1).

In 1987, Coyle *et al.* built an experimental setup to study the fountain flow effect[7]. The setup consisted of a rectangular sleeve and a plunger. The sleeve moved with constant speed, and the plunger remained stationary. By means of this experimental set-up, the kinematics of the flow were studied using tracers. They also simulated the phenomenon using a Galerkin Finite Element analysis obtaining good agreement with the experimental results. Given the settings of the experimental set-up, body forces were of importance and were included in the simulations. The effect of gravity was mainly to flatten the front.

The fountain flow effect with viscoelastic fluids in transient conditions was first considered by Mavridis *et al.* in 1988 [23] showing good agreement with the birefrigence patterns observed experimentally. The works of Mavridis show that linear fluid elements in the centerline of the flow, stretched and

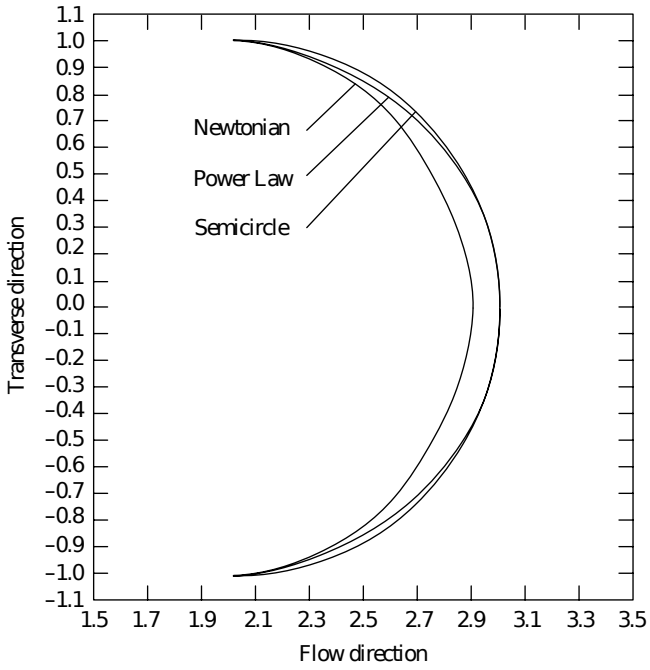

Figure 2.1: Comparison of advancing front shapes for Newtonian and power law fluids(planar geometry) Power law parameters: $n = 0.5$, $k = 10000 Pa.s^n$, $\dot{\gamma} = 500 s^{-1}$[24].

deformed attaining a "V" shape when the element passed through the fountain flow region. Beris [4] used arguments based on the continuity equation to demonstrate that those V-shaped patterns would exist regardless of the fluid rheology.

In 1990, Vroonhoven [40] developed an analytical solution for the fountain flow effect (Newtonian case) using conformal mapping in a complex plane and solving a Hilbert problem.

In 1995, Sato and Richardson [36] developed simulations for Oldroyd-B fluids explaining the role of viscoelasticity in the existence of the birefringence patterns observed by Kamal and Tan [13].

In 2004, Bogaerds simulated the instabilities of the flow front associated to injection defects characterized by differences in reflectivity of the surface of molded parts. He also demonstrated that the shape of the front is basically semiricircular for Weissenberg numbers varying between 0.1 and 2.5 [5].

In 2005, Gramberg addressed the problem of thermally induced instabilities obtaining an analytical solution to model that phenomenon [11].

Another important author with important contributions to the simulation of the fountain flow effect is Mitsoulis, who developed solutions for pseudoplastic, viscoplastic fluids [28] and viscoelastic fluids[27]. Using FEM, Mitsoulis was able to simulate the fountain flow effect in power law fluids with $n = 0.26$ (planar geometry) showing that the assumption that the front flow is approximately semicircular is not adequate for low values of n.

The simulation of the fountain flow effect is challenging because of two reasons: first, there is of a stress singularity in the pressure field and therefore in the stress field that occurs in the point of contact between the front and the wall[19] (the presence of the singularity can clearly be seen in Figures 2.2 and 2.3); second, being a free surface problem, the position of the flow front is not known a priori and iterative methods should be used in order to determine it.

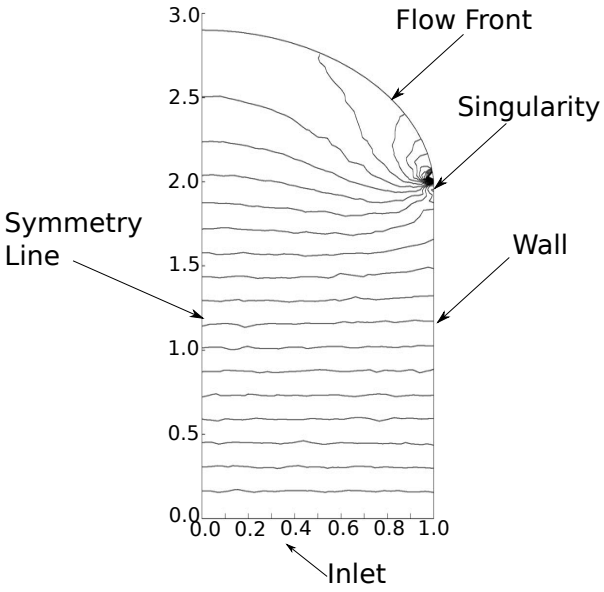

Figure 2.2: Pressure distribution in the region of the fountain flow (contour plot) [12].

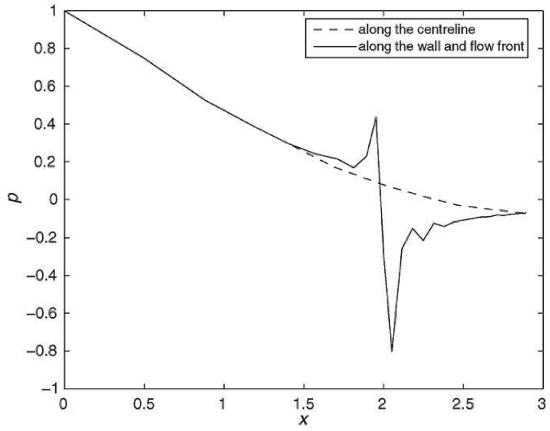

Figure 2.3: Pressure distribution along the wall, the free surface and the centerline for the fountain flow in a slit (Newtonian fluid) [12].

.

Chapter 3

The Radial Functions Method (RFM)

The interpolation of scattered data by means of radial basis functions is the basis required to develop the solution of PDEs (partial differential equations) by means of radial basis function collocation. Given a set of data $(\mathbf{x}_i, \mathbf{y}_i)$, with $i = 1, \ldots, N$, $\mathbf{x_i} \in \mathbb{R}^s$ and $\mathbf{y_i} \in \mathbb{R}$, the interpolation problem consists of finding a function $f(\mathbf{x}_i) = \mathbf{y}_i$. In the case of radial basis function interpolation, that function is given by the linear combination of the functions $\phi(r_{ij})$ and a set of augmentation polynomials:

$$f(\mathbf{x}_i) = \sum_{j=1}^{N} \alpha_j \phi(r_{ij}) + \sum_{k=1}^{t} \beta_k p_k(\mathbf{x}_i) = \mathbf{y}_i \tag{3.1}$$

Where α_j and β_k are the interpolation coefficients, $\mathbf{x}_j$ are the centers used for the interpolation, $\mathbf{x}_i$ are the collocation points, $r_{ij} = \| \mathbf{x}_i - \mathbf{x}_j \|$ is the euclidean norm or distance between the collocation points and the centers, and $\{p_k\}_{k=1}^{t}$ is a basis for $\mathcal{P}_{m-1}$ (the set of polynomials in s variables of degree equal or less than $m-1$). It is important to note that the set of collocation points need not be the same as the set of centers. However, using the same set of points is a common practice.

Chen [6]states that, theoretically, in order to have a safe reconstruction, polynomial terms of at least degree $m-1$ should be included. However, several authors [30, 21, 18, 20] have implemented the Radial Functions Method with success without including the polynomial terms at all. Larsson and Fornberg [18] state that in the case of elliptical PDEs the differences in ac-

Gaussian	$\phi(r) = e^{-cr^2}$	$c > 0$
Inverse Multiquadrics	$\phi(r) = (r^2 + c^2)^{-\beta/2}$	$c > 0 > \beta$
Sobolev Splines	$\phi(r) = K_V(r)\, r^v$	K_V is a spherical Bessel function, $v > 0$
Linear	$\phi(r) = r$	$m = 1$
Cubic	$\phi(r) = r^3$	$m = 2$
Thin Plate Spline (TPS)	$\phi(r) = r^{2a} \log r$	$2a = \beta, \beta \in 2\mathbb{Z}$, $m > \beta/2$
Polyharmonic Splines	$\phi(r) = r^\beta$	$\beta \in \mathbb{R}_{>0} \backslash 2\mathbb{Z}$, $m \geq \lceil \beta/2 \rceil$
Multiquadrics (MQ)	$\phi(r) = (r^2 + c^2)^{\beta/2}$	$\beta \in \mathbb{R}_{>0} \backslash 2\mathbb{Z}$, $c > 0$, $m \geq \lceil \beta/2 \rceil$

Table 3.1: List of common Radial Basis Functions [14, 6].

curacy and precision when the augmentation polynomials are included are relatively small. The most common RBFs and the recommended values for m are presented in Table 3.1.

The interpolation problem is reduced to solving the following equations system:

$$\begin{bmatrix} \mathbf{\Phi} & \mathbf{P} \\ \mathbf{P}^T & \mathbf{0} \end{bmatrix} \begin{bmatrix} \boldsymbol{\alpha} \\ \boldsymbol{\beta} \end{bmatrix} = \begin{bmatrix} \mathbf{Y} \\ \mathbf{0} \end{bmatrix} \tag{3.2}$$

Where,

$$\mathbf{\Phi} = \begin{bmatrix} \phi(r_{11}) & \phi(r_{12}) & \dots & \phi(r_{1N}) \\ \phi(r_{21}) & \phi(r_{22}) & \dots & \phi(r_{2N}) \\ \vdots & \vdots & \ddots & \vdots \\ \phi(r_{N1}) & \phi(r_{N2}) & \dots & \phi(r_{NN}) \end{bmatrix} \tag{3.3}$$

$$\mathbf{P} = \begin{bmatrix} p_1(x_1) & p_2(x_1) & \dots & p_t(x_1) \\ p_1(x_2) & p_2(x_2) & \dots & p_t(x_2) \\ \vdots & \vdots & \ddots & \vdots \\ p_1(x_N) & p_2(x_N) & \dots & p_t(x_N) \end{bmatrix} \tag{3.4}$$

$$\boldsymbol{\alpha}^T = \begin{bmatrix} \alpha_1, & \alpha_2 & \dots & \alpha_N \end{bmatrix}^T \tag{3.5}$$

$$\boldsymbol{\beta}^T = \begin{bmatrix} \beta_1, & \beta_2 & \dots & \beta_t \end{bmatrix}^T \tag{3.6}$$

$$\mathbf{Y}^T = \left[\begin{array}{cccc} y_1, & y_2 & \dots & y_N \end{array} \right]^T \tag{3.7}$$

The coefficients α and β can be found using any standard technique for solving systems of linear equations. Then, for an arbitrary point $\mathbf{x}$ inside the domain, the value of the function $\mathbf{y}(\mathbf{x})$, can be estimated as follows:

$$\mathbf{y}(\mathbf{x}) \approx \sum_{j=1}^{N} \alpha_j \phi \left(\| \mathbf{x} - \mathbf{x}_j \| \right) + \sum_{k=1}^{t} \beta_k p_k \left(\mathbf{x} \right) \tag{3.8}$$

Furthermore, the value of a linear differential operator $\mathcal{L}$ acting on $\mathbf{y}$ can also be approximated as:

$$\mathcal{L}\mathbf{y}(\mathbf{x}) \approx \sum_{j=1}^{N} \alpha_j \mathcal{L}\phi \left(\| \mathbf{x} - \mathbf{x}_j \| \right) + \sum_{k=1}^{t} \beta_k \mathcal{L}p_k \left(\mathbf{x} \right) \tag{3.9}$$

Then, the solution of PDEs is the next step. Let us consider two differential operators $\mathcal{L}$ and $\mathcal{B}$ associated to a partial differential equation to be solved in a domain Ω and a boundary condition to be enforced in Γ, respectively.

$$\mathcal{L}\mathbf{y}(\mathbf{x}_i) = f_i, \forall \mathbf{x}_i \in \Omega \tag{3.10}$$

$$\mathcal{B}\mathbf{y}(\mathbf{x}_i) = g_i, \forall \mathbf{x}_i \in \Gamma \tag{3.11}$$

Then, for the points in the interior of the domain and the boundary, both differential operators can be expressed using radial basis functions:

$$\sum_{j=1}^{N} \alpha_j \mathcal{L}\phi \left(r_{ij} \right) + \sum_{k=1}^{t} \beta_k \mathcal{L}p_k \left(\mathbf{x}_i \right) = f_i, \forall \mathbf{x}_i \in \Omega \tag{3.12}$$

$$\sum_{j=1}^{N} \alpha_j \mathcal{B}\phi \left(r_{ij} \right) + \sum_{k=1}^{t} \beta_k \mathcal{B}p_k \left(\mathbf{x}_i \right) = g_i, \forall \mathbf{x}_i \in \Gamma \tag{3.13}$$

The resulting system of equations can be represented schematically as follows [33]:

$$\left[\begin{array}{cc} \mathcal{L}\mathbf{\Phi}_\Omega & \mathcal{L}\mathbf{P}_\Omega \\ \mathcal{B}\mathbf{\Phi}_\Gamma & \mathcal{B}\mathbf{P}_\Gamma \\ \mathbf{P}^T & \mathbf{0} \end{array} \right] \left[\begin{array}{c} \boldsymbol{\alpha} \\ \boldsymbol{\beta} \end{array} \right] = \left[\begin{array}{c} \mathbf{f} \\ \mathbf{g} \\ \mathbf{0} \end{array} \right] \tag{3.14}$$

In order to demonstrate the application of the method with a relatively simple example, the solution of the Poisson equation

$$-\nabla^2 u\,(x,y) = f\,(x,y) \tag{3.15}$$

that describes the 2D heat transfer by conduction in a plate with an internal heat generation $f(x,y)$ is considered. Two boundary conditions were implemented:

- Dirichlet, when the temperatures are known in the boundary(Γ_1)

$$u(x,y) = g(x,y) \tag{3.16}$$

- Neumann, when the heat flux is known in the boundary (Γ_2)

$$\frac{\partial u(x,y)}{\partial n} = q(x,y) \tag{3.17}$$

Using RFM, the resulting system of equations can be expressed schematically as:

$$\begin{bmatrix} \nabla^2\boldsymbol{\Phi}_{\boldsymbol{\Omega}} & \nabla^2\mathbf{P}_{\boldsymbol{\Omega}} \\ \boldsymbol{\Phi}_{\boldsymbol{\Gamma_1}} & \mathbf{P}_{\boldsymbol{\Gamma_1}} \\ \frac{\partial\boldsymbol{\Phi}_{\boldsymbol{\Gamma_2}}}{\partial\mathbf{n}} & \frac{\partial\mathbf{P}_{\boldsymbol{\Gamma_2}}}{\partial\mathbf{n}} \\ \mathbf{P}^T & \mathbf{0} \end{bmatrix} \begin{bmatrix} \boldsymbol{\alpha} \\ \boldsymbol{\beta} \end{bmatrix} = \begin{bmatrix} -\mathbf{f} \\ \mathbf{g} \\ \mathbf{q} \\ \mathbf{0} \end{bmatrix} \tag{3.18}$$

For this problem, a comparison was made between different radial basis functions by Ramírez *et al.*[34]. A FEM solution based in triangular elements and first degree Lagrange polynomials as found in [9] was also developed and is presented for comparison purposes. The meshing was done using the program TRIANGLE[38]. In order to assess the accuracy of the method for this particular equation, two domains with different geometries were studied (Figure 3.1). For each domain, known functions $u(x,y)$ were chosen as solutions of the Poisson equation(Figure 3.2):

- Domain 1
  - $u(x,y) = \sin(\pi x)\cos(\frac{\pi}{2}y) + 10$
  - $u(x,y) = \sin(2\pi x)\cos(\pi y) + 10$
  - $u(x,y) = \sin(4\pi x)\cos(2\pi y) + 10$

- Domain 2
  - $u(x,y) = \sin(\frac{\pi}{20}x) + \cos(\frac{\pi y}{20}) + 10$
  - $u(x,y) = \sin(\frac{\pi}{10}x) + \cos(\frac{\pi y}{10}) + 10$
  - $u(x,y) = \sin(\frac{\pi}{5}x) + \cos(\frac{\pi y}{5}) + 10$

Then, the fountain functions $f(x,y)$ were calculated by applying the laplacian operator ∇^2 to the selected functions $u(x,y)$. Neumann and Dirichlet boundary conditions were found by calculating the directional derivative $\frac{\partial u(x,y)}{\partial n}$ and by evaluating the functions $u(x,y)$ respectively. By doing so, complete boundary problems with known analytical solutions were obtained.

These problems were solved by means of the Radial Functions Method (RFM) and the Finite Element Method (FEM) and compared to the original $u(x,y)$ functions which correspond to the analytical solutions. For the RFM, two functions were used: the thin plate spline (TPS) and the multiquadrics (with $\beta = 1$). In order to be able to compare the different solutions quantitatively, the following measurement of the error was defined:

$$Error = \frac{\parallel \mathbf{u}_{analytical} - \mathbf{u}_{numerical} \parallel}{\parallel \mathbf{u}_{analytical} \parallel} \tag{3.19}$$

Where $\mathbf{u}_{analytical}$ and $\mathbf{u}_{numerical}$ and are vectors containing the values of u corresponding to the analytic and numerical solutions for all collocation points, and $\parallel \cdot \parallel$ is the euclidean norm.

For the TPS, polynomials of the third degree were added. According to Chen [6], the additional polynomials must have a degree of at least $m-1$ in order to ensure that the resulting system of equations has an unique solution. When applying this criterion, for the TPSs with $a = 3$ and $a = 4$, third and fourth degree polynomials must be added respectively. However, in this work all the results were obtained using third degree augmentation polynomials for the TPSs. Even without including the higher degree terms, the results obtained by means of the TPS with $a = 4$ are superior to the ones with $a = 3$. In the case of the MQ, the parameter c has a strong influence on the obtained results. Figure 3.4 shows the influence of c in the error and the condition number of the matrix. Considering, the influence of c in the error, the graph has an optimal point. The existence of this point is well known in the literature[20] and can be explained as follows: in ideal conditions (exact arithmetic) the accuracy tends to improve as the parameter c increases; nevertheless, as c gets bigger, the conditioning of the matrix tends

to worsen. Since real numbers can only be represented to a certain precision given by the floating point of the machine, the parameter cannot be increased indefinitely without losing stability. It is worth mentioning that the optimal value of the parameter c depends on several factors including the number of points, the geometry of the domain, the specific differential equation to be solved, etc. However, there is a wide range of possible values for c which will produce suitable solutions as has been reported by Li[20]. In the present work, the parameter c was taken as 10 for the domain 1 and 0.5 for the domain 2 without attempting its optimization. Regarding the accuracy, it is observed that better results were obtained by using RFM than by using FEM. However, a direct comparison is difficult to establish because the execution times differ considerably between the two implementations, being smaller for FEM.

In general, the function with the best performance in terms of the absolute errors was the MQ. Using the TPS with a parameter $a = 4$, good results were also obtained. However, even if better solutions can be obtained by using the MQ, the TPS continues to be the most practical option because no adjustable parameter is needed. The results show that the implementation of RFM with the MQ is a very interesting option but more investigation is required regarding the optimization of the characteristic parameter c.

The radial basis function collocation method has been used to simulate diverse polymer processes including non-linearities caused by the non-Newtonian behavior of polymer melts and different rheological models such as the power law, Carreau and Giesekus (viscoelastic model). In this regard, it is important to note the work of Estrada [8] and López[21] who have worked in the solution of the equations of motion and energy obtaining suitable simulations for different polymer processing problems: the flow through extrusion dies, the flow through a slit rheometer, calendering, and the thermal imbalance in the runners of injection molds.

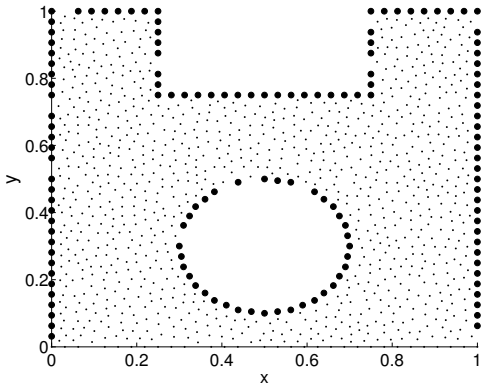

(a) Domain 1.

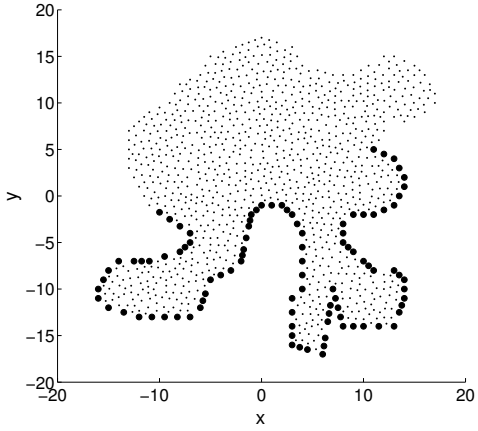

(b) Domain 2.

Figure 3.1: Geometry of the domains. The dark spots represent boundaries with the Dirichlet condition. In the remaining boundaries, von Neumann conditions were imposed.

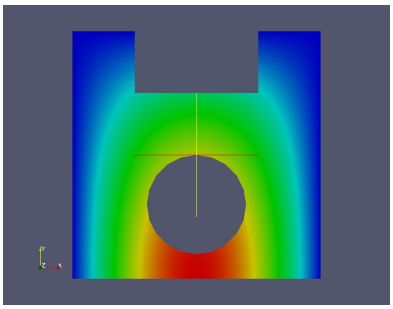

(a) $u(x, y) = \sin(\pi x)\cos(\frac{\pi}{2}y) + 10$

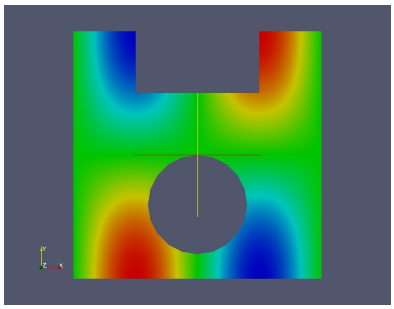

(b) $u(x, y) = \sin(2\pi x)\cos(\pi y) + 10$

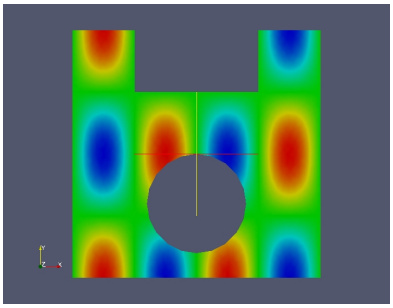

(c) $u(x, y) = \sin(4\pi x)\cos(2\pi y) + 10$

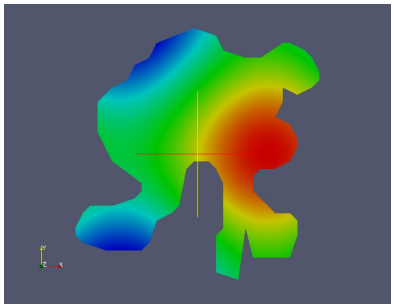

(d) $u(x, y) = \sin(\frac{\pi}{20}x) + \cos(\frac{\pi y}{20}) + 10$

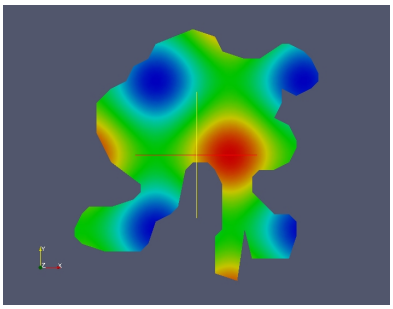

(e) $u(x, y) = \sin(\frac{\pi}{10}x) + \cos(\frac{\pi y}{10}) + 10$

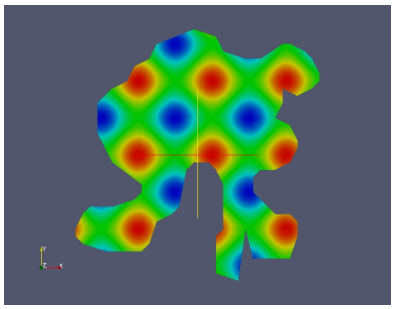

(f) $u(x, y) = \sin(\frac{\pi}{5}x) + \cos(\frac{\pi y}{5}) + 10$

Figure 3.2: Contour plots of the different functions $u(x, y)$ chosen as analytical solutions.

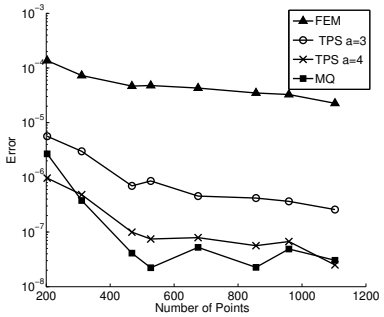

(a) $u(x,y) = \sin(\pi x)\cos(\frac{\pi}{2}y) + 10$

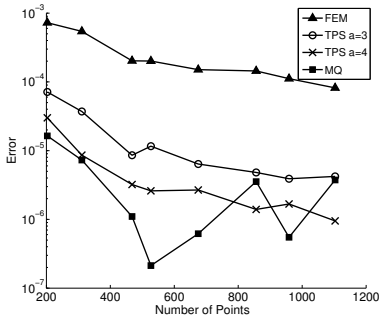

(b) $u(x,y) = \sin(2\pi x)\cos(\pi y) + 10$

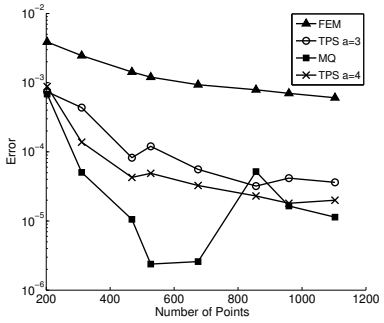

(c) $u(x,y) = \sin(4\pi x)\cos(2\pi y) + 10$

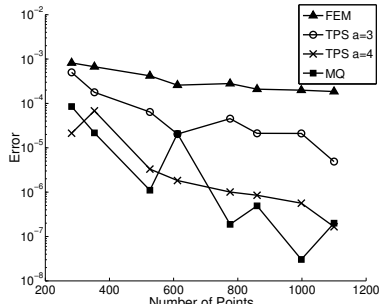

(d) $u(x,y) = \sin(\frac{\pi}{20}x) + \cos(\frac{\pi y}{20}) + 10$

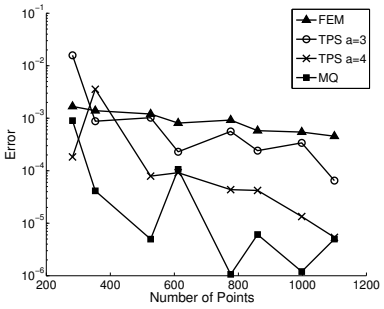

(e) $u(x,y) = \sin(\frac{\pi}{10}x) + \cos(\frac{\pi y}{10}) + 10$

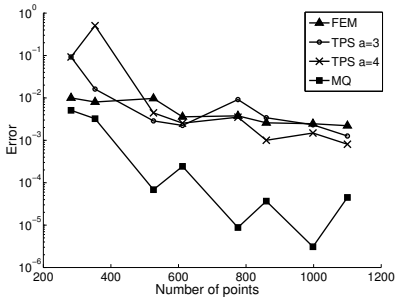

(f) $u(x,y) = \sin(\frac{\pi}{5}x) + \cos(\frac{\pi y}{5}) + 10$

Figure 3.3: Errors as a function of the number of points for the different Poisson equation problems solved in domain 1 (a, b, c) and domain 2 (d, e, f).

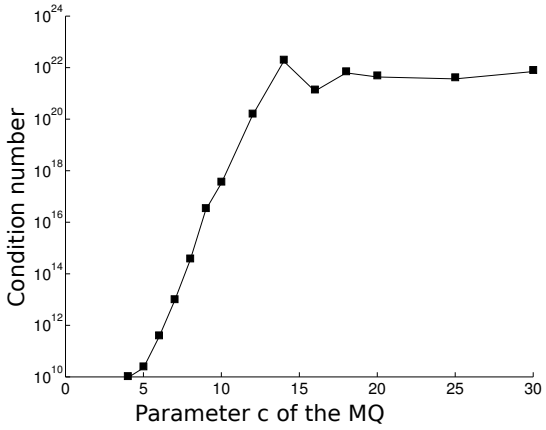

(a) Parameter c vs. Condition number

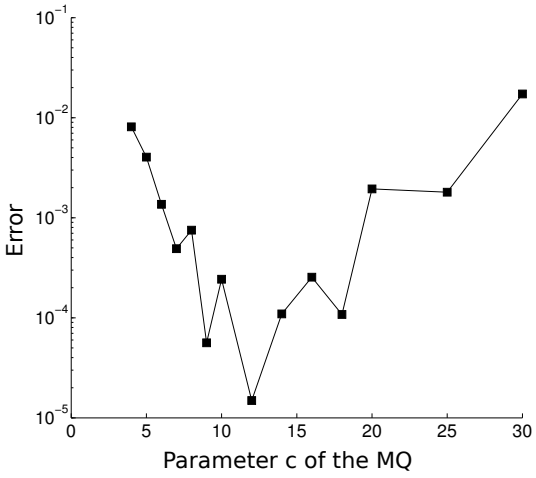

(b) Parameter c vs. Error

Figure 3.4: Influence of the parameter c on the error and the condition number of the matrix (domain 2, 612 collocation points, $u(x, y) = \sin(\frac{\pi}{5}x) + \cos(\frac{\pi y}{5}) + 10$).

Chapter 4

Implementation and Results

4.1 Newtonian Case in a Slit

4.1.1 Modeling

The problem that is considered is the modeling and simulation of the fountain flow in a planar slit. This kind of flow is typical in injection molded parts with high aspect ratios between the width and the thickness, allowing the reduction of the domain to a 2D geometry. The coordinate system, geometry of the domain and the corresponding boundary conditions are shown in Figure 4.1. In this case, there is no velocity or gradients in the z direction. Assuming that the fluid is incompressible, the equation of continuity can be simplified as follows (equation 4.1):

$$\frac{\partial u_{x_i}}{\partial x} + \frac{\partial u_{y_i}}{\partial y} = 0 \tag{4.1}$$

Since inertia terms and body forces are negligible in the injection molding process, and considering only the Newtonian, isothermal case, the motion equations can be written as (equations 4.2 and 4.3):

$$0 = -\frac{\partial p_i}{\partial x} + \mu \nabla^2 u_{x_i} \tag{4.2}$$

$$0 = -\frac{\partial p_i}{\partial y} + \mu \nabla^2 u_{y_i} \tag{4.3}$$

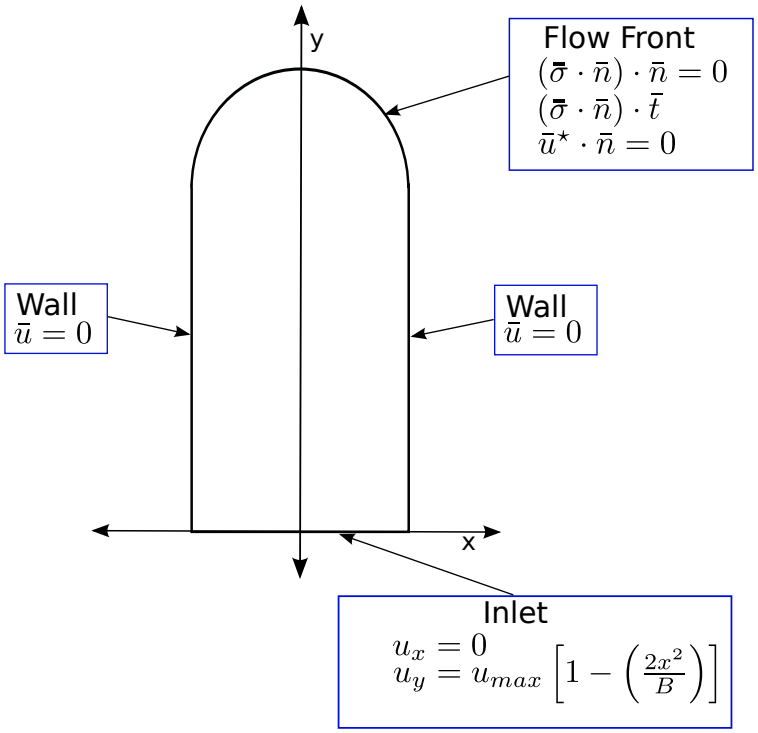

Figure 4.1: Boundary conditions for the simulation of the fountain flow effect.

Non-slip conditions ($\bar{u} = 0$) are assumed in both walls. At the inlet a parabolic velocity profile (corresponding to a developed pressure flow) is assumed. In the flow front, the boundary conditions are given by the vanishing tangential stresses (equation 4.4) [28]

$$(\bar{\bar{\sigma}} \cdot \bar{n}) \cdot \bar{t} = 0 \tag{4.4}$$

and the normal stress must satisfy a force equilibrium given by equation 4.5 [29].

$$(\bar{\bar{\sigma}} \cdot \bar{n}) \cdot \bar{n} = -2R_c\gamma - p_0 \tag{4.5}$$

Where, $\bar{t}$ and $\bar{n}$ are the tangential and normal vectors to the surface, $\bar{\bar{\sigma}}$ is the total stress tensor, $2R_c$ is the mean surface curvature, γ is the surface tension, and p_0 is the reference pressure in the cavity.

In injection molding, the superficial tension is negligible when compared to the viscous forces[15]. Besides, without loss of generality, the reference pressure can be set to zero obtaining equation 4.6 which can also be found in references [28, 37].

$$(\bar{\bar{\sigma}} \cdot \bar{n}) \cdot \bar{n} = 0 \tag{4.6}$$

If a reference system that moves at the average velocity of the flow is considered, there is no flow through the front surface (equation 4.7) [28].

$$\bar{u^\star} \cdot \bar{n} = 0 \tag{4.7}$$

Where $\bar{u^\star}$ is the velocity vector in the comoving reference system for each of the flow front points. This kinematic boundary condition was not enforced via collocation, but attained as a result of an iterative process devised to find the shape of the flow front.

4.1.2 Numerical Implementation

The numerical implementation is based on the Radial Functions Method (RFM). The primary variables in this problem when solving the balance equations are the pressure and velocity components. These variables can be approximated using the Radial Functions Method as follows (equations 4.8, 4.9, 4.10):

$$u_{x_i} = \sum_{j=1}^{N} \phi_u \left(r_{ij}\right) \lambda_j \tag{4.8}$$

$$u_{y_i} = \sum_{j=1}^{N} \phi_u \left(r_{ij}\right) \xi_j \tag{4.9}$$

$$p_i = \sum_{j=1}^{N_p} \phi_p \left(r_{ij}\right) \beta_j \tag{4.10}$$

Using the RFM notation, the continuity and motion equations can be approximated according to equations 4.11, 4.12, 4.13 [21, 30].

$$\sum_{j=1}^{N} \left[\frac{\partial \phi_u \left(r_{ij}\right)}{\partial r} \frac{\partial r_{ij}}{\partial x} \right] \lambda_j + \sum_{j=1}^{N} \left[\frac{\partial \phi_u \left(r_{ij}\right)}{\partial r} \frac{\partial r_{ij}}{\partial y} \right] \xi_j = 0 \tag{4.11}$$

$$0 = -\sum_{j=1}^{N_p} \left[\frac{\partial \phi_p}{\partial r} \frac{\partial r_{ij}}{\partial x} \right] \beta_j + \sum_{j=1}^{N} \left[\mu \nabla^2 \phi_u \left(r_{ij}\right) \right] \lambda_j \tag{4.12}$$

$$0 = -\sum_{j=1}^{N_p} \left[\frac{\partial \phi_p}{\partial r} \frac{\partial r_{ij}}{\partial y} \right] \beta_j + \sum_{j=1}^{N} \left[\mu \nabla^2 \phi_u \left(r_{ij}\right) \right] \xi_j \tag{4.13}$$

Where N and N_p are the number of centers corresponding to the velocity and pressure fields, respectively. In references [21, 30] there is a detailed account of the implementation of the RFM for non-Newtonian and non-isothermal cases.

The Dirichlet boundary conditions for the velocity field (in the walls and entry) can also be represented using radial basis functions as (equations 4.14 and 4.15):

$$\sum_{j=1}^{N} \lambda_j \phi_u \left(r_{ij}\right) = u_{a_x}; i \in \Gamma^{D_u} \tag{4.14}$$

$$\sum_{j=1}^{N} \xi_j \phi_u \left(r_{ij}\right) = u_{a_y}; i \in \Gamma^{D_u} \tag{4.15}$$

In a similar fashion, equations corresponding to the vanishing stresses in the flow front can be expanded and approximated using radial basis functions (equations 4.19 and 4.22) :

$$(\bar{\bar{\sigma}} \cdot \bar{n}) \cdot \bar{n} = \sigma_{xx} {n_x}^2 + 2\sigma_{xy} n_x n_y + \sigma_{yy} {n_y}^2 \tag{4.16}$$

$$0 = \left[-2\mu \frac{\partial u_x}{\partial x} + p \right] {n_x}^2 - 2\mu \left[\frac{\partial u_y}{\partial x} + \frac{\partial u_x}{\partial y} \right] n_x n_y + \left[-2\mu \frac{\partial u_y}{\partial y} + p \right] {n_y}^2 \tag{4.17}$$

$$0 = -2\mu \left[\frac{\partial u_x}{\partial x} n_x^2 + n_x n_y \left(\frac{\partial u_y}{\partial x} + \frac{\partial u_x}{\partial y} \right) + \frac{\partial u_y}{\partial y} n_y^2 \right] + p \left(n_x^2 + n_y^2 \right) \tag{4.18}$$

$$\begin{aligned} 0 = \left(n_x^2 + n_y^2 \right) \sum_{j=1}^{N_p} \beta_j \phi_p \left(r_{ij} \right) - \sum_{j=1}^{N} 2\lambda_j \mu \frac{\partial \phi_u \left(r_{ij} \right)}{\partial r} \left(\frac{\partial r_{ij}}{\partial x} n_x^2 + \frac{\partial r_{ij}}{\partial y} n_x n_y \right) \\ - \sum_{j=1}^{N} 2\xi_j \mu \frac{\partial \phi_u \left(r_{ij} \right)}{\partial r} \left(\frac{\partial r_{ij}}{\partial y} n_y^2 + \frac{\partial r_{ij}}{\partial x} n_x n_y \right) \end{aligned} \tag{4.19}$$

$$(\bar{\bar{\sigma}} \cdot \bar{n}) \cdot \bar{t} = \sigma_{xx} n_x t_x + \sigma_{xy} n_y t_x + \sigma_{yx} n_x t_y + \sigma_{yy} n_y t_y \tag{4.20}$$

$$\begin{aligned} 0 = -\mu \left[2 \frac{\partial u_x}{\partial x} n_x t_x + \left(n_y t_x + n_x t_y \right) \left(\frac{\partial u_y}{\partial x} + \frac{\partial u_x}{\partial y} \right) + 2 \frac{\partial u_y}{\partial y} n_y t_y \right] \\ + p \left(n_x t_x + n_y t_y \right) \end{aligned} \tag{4.21}$$

$$\begin{aligned} 0 = \sum_{j=1}^{N} \lambda_j \mu \frac{\partial \phi_u \left(r_{ij} \right)}{\partial r} \left[2 \frac{\partial r_{ij}}{\partial x} n_x t_x + \frac{\partial r_{ij}}{\partial y} \left(n_y t_x + n_x t_y \right) \right] \\ + \sum_{j=1}^{N} \xi_j \mu \frac{\partial \phi_u \left(r_{ij} \right)}{\partial r} \left[2 \frac{\partial r_{ij}}{\partial y} n_y t_y + \frac{\partial r_{ij}}{\partial x} \left(n_y t_x + n_x t_y \right) \right] \end{aligned} \tag{4.22}$$

Since the form of the flow front is not known a priori, an iterative approach was implemented to determine it according to equation 4.23 [28].

$$y_{new} = y_w + \int_{B/2}^{x} \frac{u_y - U_s}{u_x} dx \tag{4.23}$$

Where y_{new} is the new position of the flow front, B is the slit width, U_s is the velocity in y of the stagnation point (located at the tip of the flow front), y_w is the position (y coordinate) of the contact point with the wall, u_y and u_x are the velocities in the flow front. When the final position of the front is attained and the kinematic condition fulfilled, U_s is equal to the average velocity of the flow and equation 4.23 corresponds to the streamline found by integrating the velocity of a particle that impinges in the contact point between the front and the wall. The initial shape of the front is assumed to be a semicircle.

4.1.3 Results

The parameters of the simulation are the following:

- Slit width (B): 2 mm
- Maximum velocity at the inlet: 1 m/s
- Viscosity: 100 Pa.s
- Domain length(without including the front): 2 mm

The collocation points for this simulation are shown in figure 4.2. Figure 4.4 shows the velocity field in a stationary and a moving reference system as vector plots. When the moving reference system is considered, the velocity vectors at the flow front are tangential to the surface according to the condition stated in equation 4.7. Figure 4.1.3 shows the obtained pressure and the velocity fields as contour plots. According to the obtained pressure distribution, the presence of a singularity in the contact point between the front and the wall is evident. The existence of this singularity point in the model is well documented in the literature [28]. At the entrance, a linear fall of the pressure is observed, which corresponds to the expected behavior in a developed pressure flow. At the tip of the flow front, the pressure drops to a value slightly below zero as has already been noticed by other researchers [28, 10]. In the literature, the change in the advancing front location is commonly described by using a dimensionless front line location, defined according to equation 4.24.

$$\chi = \frac{\delta y_{cl}}{B/2} \tag{4.24}$$

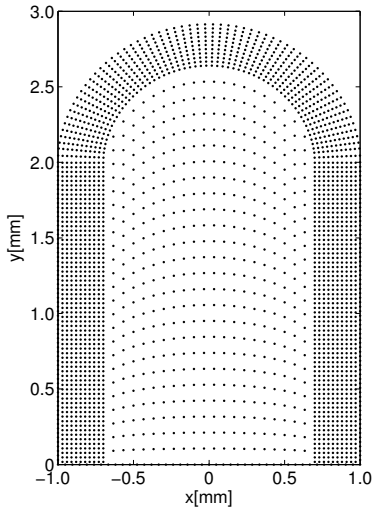

Figure 4.2: Fountain flow in a slit (Newtonian case). Domain and collocation points.

$$\delta y_{cl} = y_{cl} - y_w \tag{4.25}$$

Where y_{cl} is the difference between the y coordinate of the point of the front located at the centerline, and the point in contact with the wall. In this thesis, the obtained value for χ of was 0.91 whereas, in the past, other researchers have obtained values ranging from 0.90 to 0.94(table 4.1). Figure 4.6 shows the difference between the initially assumed shape of the front, and the final shape.

The streamlines obtained in this work are similar to the ones obtained by other authors. For instance, Figure 4.5 shows the comparison between the streamlines obtained by Huilgol [12] and the streamlines obtained in this thesis.

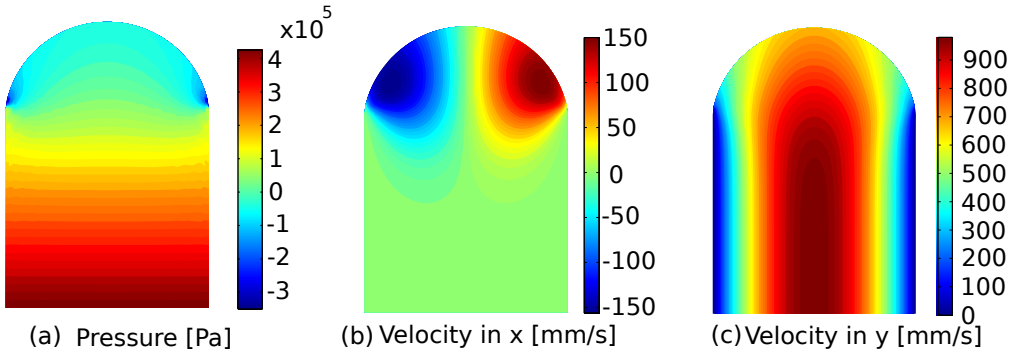

Figure 4.3: Newtonian case, pressure and velocity fields.

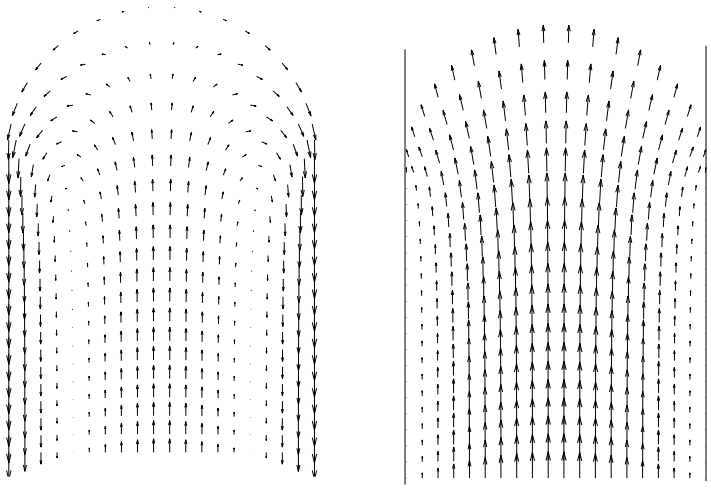

Figure 4.4: Newtonian case, velocity fields for: (a) A reference system that moves with the flow front,(b) A stationary reference system.

Researcher	**Geometry**	**Frame of reference**	χ
Mavridis et al.	Planar	Moving-steady	0.90
Coyle et al.	Planar	Moving-steady	0.93
Behrens et al.	Planar	Moving-steady	0.94
Behrens et al.	Planar	Fixed-Transient	0.91
Bogaerds et al.	Planar	Moving-steady	0.92
Mitsouils	Planar	Moving-steady	0.90
This work	Planar	Moving-steady	0.91
Mavridis et al.	Axisymmetric	Moving-steady	0.83
Behrens et al.	Axisymmetric	Moving-steady	0.82
Behrens et al.	Axisymmetric	Fixed-Transient	0.86
Behrens et al.	Axisymmetric	Exp. Result	0.83±0.04
Mitsouils	Axisymmetric	Moving-steady	0.84

Table 4.1: Values of χ for a Newtonian fluid according to different authors [28].

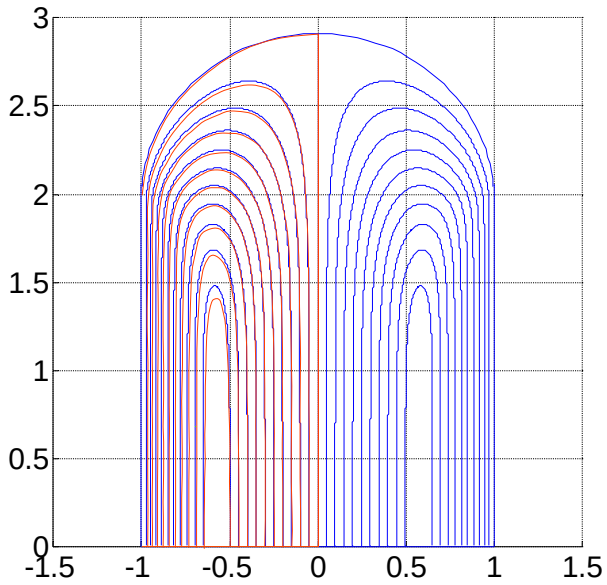

Figure 4.5: Newtonian case, comparison between the streamlines obtained by Huilgol (red)[12] and the streamlines obtained in this work (blue).

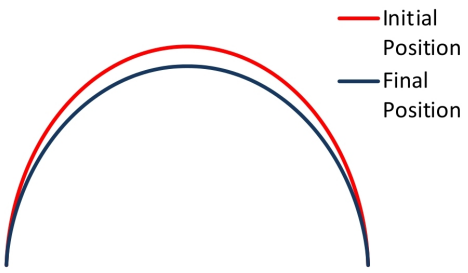

Figure 4.6: Newtonian case, difference between the initial and the final shape of the flow front.

4.2 Non-Newtonian Case in a Slit

4.2.1 Modeling and Numerical Implementation

In the non-Newtonian case, extra-terms appear in the motion equation as a result of the variation of the viscosity with the shear rate. Therefore, neglecting the inertia terms, the equations of motion for x and y can be written as (equations 4.26 and 4.27) [21, 30]:

$$0 = -\frac{\partial p_i}{\partial x} + \eta_i \nabla^2 u_{x_i} + 2\frac{\partial \eta_i}{\partial x}\frac{\partial u_{x_i}}{\partial x} + \frac{\partial \eta_i}{\partial y}\left(\frac{\partial u_{x_i}}{\partial y} + \frac{\partial u_{y_i}}{\partial x}\right) \tag{4.26}$$

$$0 = -\frac{\partial p_i}{\partial y} + \eta_i \nabla^2 u_{y_i} + 2\frac{\partial \eta_i}{\partial y}\frac{\partial u_{y_i}}{\partial y} + \frac{\partial \eta_i}{\partial x}\left(\frac{\partial u_{y_i}}{\partial x} + \frac{\partial u_{x_i}}{\partial y}\right) \tag{4.27}$$

and approximated using radial basis functions as (equations 4.28 and 4.29)

$$\begin{aligned} 0 = \sum_{j=1}^{N} \left[-\eta_i \nabla^2 \phi_u\left(r_{ij}\right) - \frac{\partial \phi_u\left(r_{ij}\right)}{\partial r}\left(2\frac{\partial \eta_i}{\partial x}\frac{\partial r_{ij}}{\partial x} + \frac{\partial \eta_i}{\partial y}\frac{\partial r_{ij}}{\partial y}\right)\right] \lambda_j \\ + \sum_{j=1}^{N} \left[-\frac{\partial \phi_u\left(r_{ij}\right)}{\partial r}\frac{\partial \eta_i}{\partial y}\frac{\partial r_{ij}}{\partial y}\right] \xi_j + \sum_{j=1}^{N_p} \left[\frac{\partial \phi_p\left(r_{ij}\right)}{\partial r}\frac{\partial r_{ij}}{\partial x}\right] \beta_j \end{aligned} \tag{4.28}$$

$$0 = \sum_{j=1}^{N} \left[-\eta_i \nabla^2 \phi_u \left(r_{ij} \right) - \frac{\partial \phi_u \left(r_{ij} \right)}{\partial r} \left(2 \frac{\partial \eta_i}{\partial y} \frac{\partial r_{ij}}{\partial y} + \frac{\partial \eta_i}{\partial x} \frac{\partial r_{ij}}{\partial x} \right) \right] \xi_j + \sum_{j=1}^{N} \left[-\frac{\partial \phi_u \left(r_{ij} \right)}{\partial r} \frac{\partial \eta_i}{\partial x} \frac{\partial r_{ij}}{\partial y} \right] \lambda_j + \sum_{j=1}^{N_p} \left[\frac{\partial \phi_p \left(r_{ij} \right)}{\partial r} \frac{\partial r_{ij}}{\partial y} \right] \beta_j \tag{4.29}$$

In order to calculate the derivatives of the viscosity, two approaches have been used. In the first, the derivatives are calculated simply by applying RFM on the viscosity field itself (equation 4.31):

$$\eta_i = \sum_{j=1}^{N} \phi_\eta \left(r_{ij} \right) \omega_j \tag{4.30}$$

$$\frac{\partial \eta_i}{\partial x} = \sum_{j=1}^{N} \frac{\partial \phi_\eta \left(r_{ij} \right)}{\partial r} \frac{\partial r}{\partial x} \omega_j \tag{4.31}$$

In the second approach, the spatial derivative of the viscosity is expressed in terms of the derivative of the shear rate using the chain rule (equation 4.32):

$$\frac{\partial \eta}{\partial x} = \frac{\partial \eta}{\partial |\dot{\gamma}|} \frac{\partial |\dot{\gamma}|}{\partial x} \tag{4.32}$$

The derivative of the shear rate can the be approximated using radial functions (equation 4.33):

$$\frac{\partial |\dot{\gamma}|_i}{\partial x} = \sum_{j=1}^{N} \frac{\partial \phi_{\dot{\gamma}} \left(r_{ij} \right)}{\partial r} \frac{\partial r}{\partial x} \varsigma_j \tag{4.33}$$

The derivative of the viscosity in y can be approximated similarly. For the power law constitutive equation, the viscosity is equal to infinity when the shear rate is zero. For this reason, the shear rate field is better bounded and, therefore, the second approach is preferred and used in this work.

The viscosity is a function of the shear rate and therefore of the velocity field. Hence, the viscosity field is initially unknown and must be found using an iterative approach. Initially the viscosity is assumed to be constant in the domain (Newtonian fluid). Then the velocity field is calculated according to equations 4.11, 4.28 and 4.29. This information is used to recalculate the

viscosity by using equations 4.32 and 4.33. This process is repeated until convergence is attained. In this work, the viscosity is assumed to vary with the shear rate according to a power law relationship (equation 4.34). The Carreau model, which is more realistic, has also been implemented. However, since the power-law constitutive equation is popular in the literature, it is used for comparison purposes.

$$\eta = k|\dot{\gamma}|^{n-1} \tag{4.34}$$

In order to improve the accuracy of the solution, a numerical scheme based in double collocation with phantom points was implemented. The double collocation consists in enforcing not only the boundary conditions but also the continuity and motion equations in the boundary points. In order to obtain a square matrix, it is necessary to increase the number of centers by adding phantom points outside the domain near the boundaries. The details about the implementation of this numerical technique can be found in [21].

4.2.2 Results

For this set of simulations, the power law parameter k was set as $1000Pa \cdot s^n$, and the boundary condition at the inlet corresponds to the velocity profile of a pressure driven flow in a slit for a power law fluid (equation 4.35), where u_{ave} is the average velocity of the flow and was set at $0.666m/s$.

$$u_y = u_{ave}\left(\frac{1+2n}{1+n}\right)\left[1 - \left|\frac{2x}{B}\right|^{\frac{1}{n}+1}\right] \tag{4.35}$$

Mavridis[24], the first author to simulate the fountain flow effect for a power law fluid, found that for $1.0 \geq n \geq 0.5$, the kinematics were remarkably similar to the Newtonian case. Furthermore, as n decreases, the flow front tends to move forwards by a small amount and is almost semicircular for $n = 0.5$. These general trends were also observed in the simulations of the present work, where the fountain flow was simulated between $1.1 \geq n \geq 0.6$. Figure 4.7 shows the streamlines for the case where $n = 0.6$, demonstrating that the pattern formed by the the streamlines is similar to the Newtonian case. Figures 4.8 and 4.9 show the dimensionless center line position and the shape of the front for different values of n and a good agreement with the results of Mavridis (see Figure 2.1).

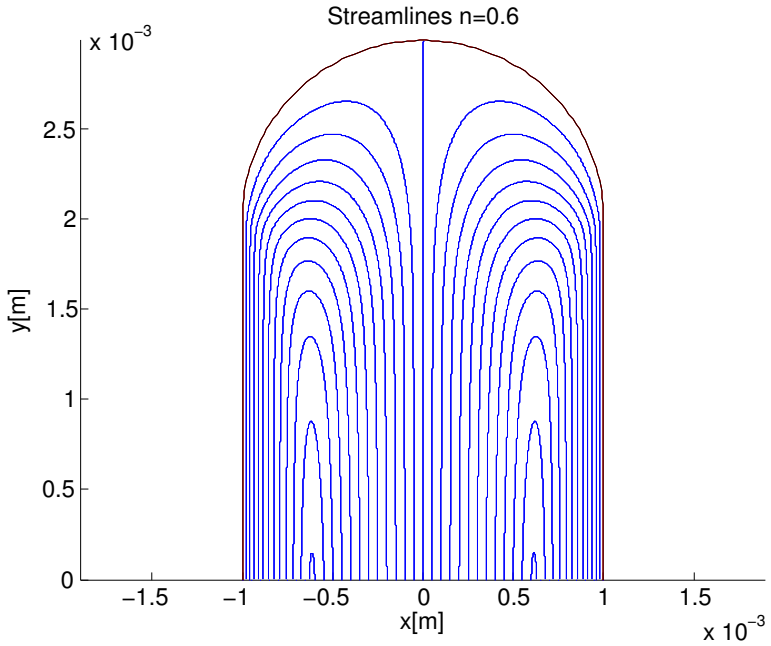

Figure 4.7: Streamlines for a power-law parameter of $n = 0.6$.

Recently (2010), Mitsoulis[28] was able to simulate fountain flow effect in steady state for lower values of n (the minimum value of his simulations was $n = 0.26$ for a slit), and concluded that the flow front continues to advance but no longer ressembles a semicircle.

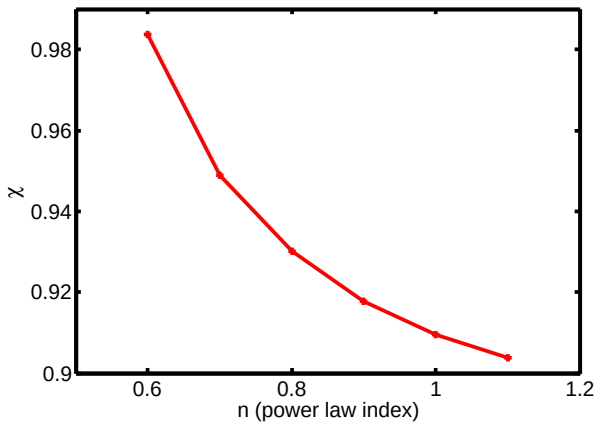

Figure 4.8: Dimensionless centerline location as a function of the power law parameter n.

In order to validate the results, the motion and continuity equations were solved by means of finite elements [1] using COMSOL 4.0. For the comparison, the front shape was not iterated and was considered to be a semicircle. An attempt to solve a similar problem with iteration of the front using the same commercial software has been attempted by Al-Zain [1] with limited success, since the iteration of the front did not lead to the fulfillment of the kinematic condition $\bar{u}^\star \cdot \bar{n} = 0$ and therefore the fountain flow effect could not be fully captured. For the case where the front was assumed to be a semicircle and no iteration of its shape was attempted, there was good agreement between the solutions obtained by both methods. Figures 4.11 to 4.16 show the comparison between the velocity and pressure fields obtained by FEM and RFM for tree sections of the domain (Figure 4.10).

In Figures 4.13(b) and 4.16(b), given the symmetry of the problem, the x velocity should be zero. Although the absolute values of the velocities

[1]The author acknowledges the help of Jorge Iván Villegas of the ICIPC in the development of the COMSOL simulations.

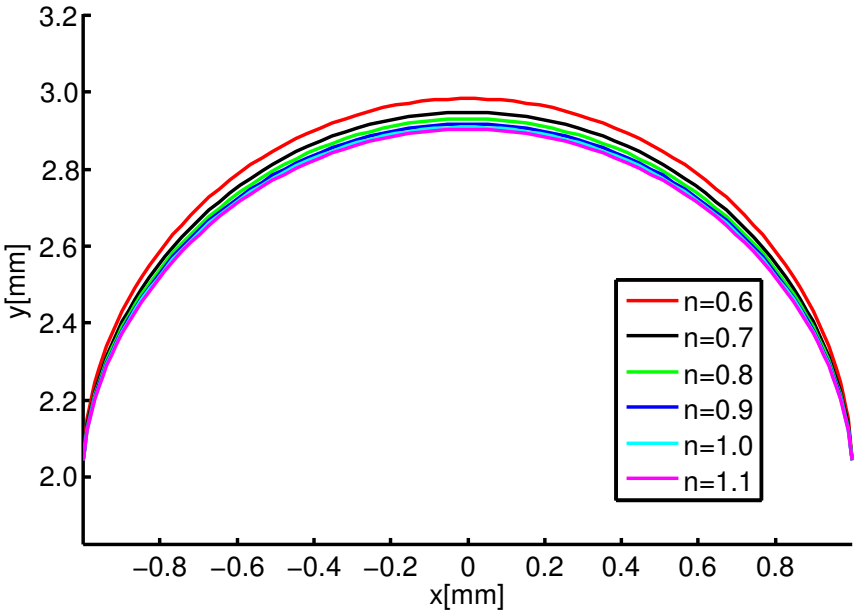

Figure 4.9: Shape of the flow front for different values of the power law parameter n.

obtained by using FEM are smaller than the ones obtained using RFM, both of them are several orders of magnitude smaller that the average velocity of the flow.

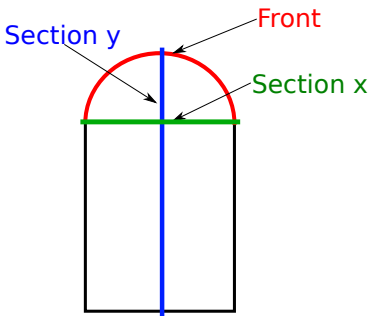

Figure 4.10: Sections taken for the comparison between the solution obtained using RFM and FEM (COMSOL).

4.3 Newtonian-Axisymmetric Case with Body Forces

4.3.1 Modeling and Numerical Implementation

Al-Zain and Osswald [1]designed and built and experimental setup for the simulation of the fountain flow effect in order to study its influence in the fiber distribution and orientation in injection molded parts (Figures 4.17 and 4.18). The device consists of a transparent sleeve filled with silicon oil and a stationary plunger. A cluster of fibers is positioned inside the sleeve near the plunger at the beginning of the experiment. As the sleeve moves downwards, a fountain flow develops near the free surface. In this way, the trajectory of the fibers as they move through the front region can be observed and studied.

In this experimental setup, the existence of bodyforces due to gravity cannot be ignored. Given the axial symmetry of the setup, considering a steady state and assuming negligible inertia forces (the Reynolds numbers are low given the high viscosity of the silicone oil and the low velocity of the walls), the continuity and motion equations can be simplified as (equations 4.36, 4.37, 4.38):

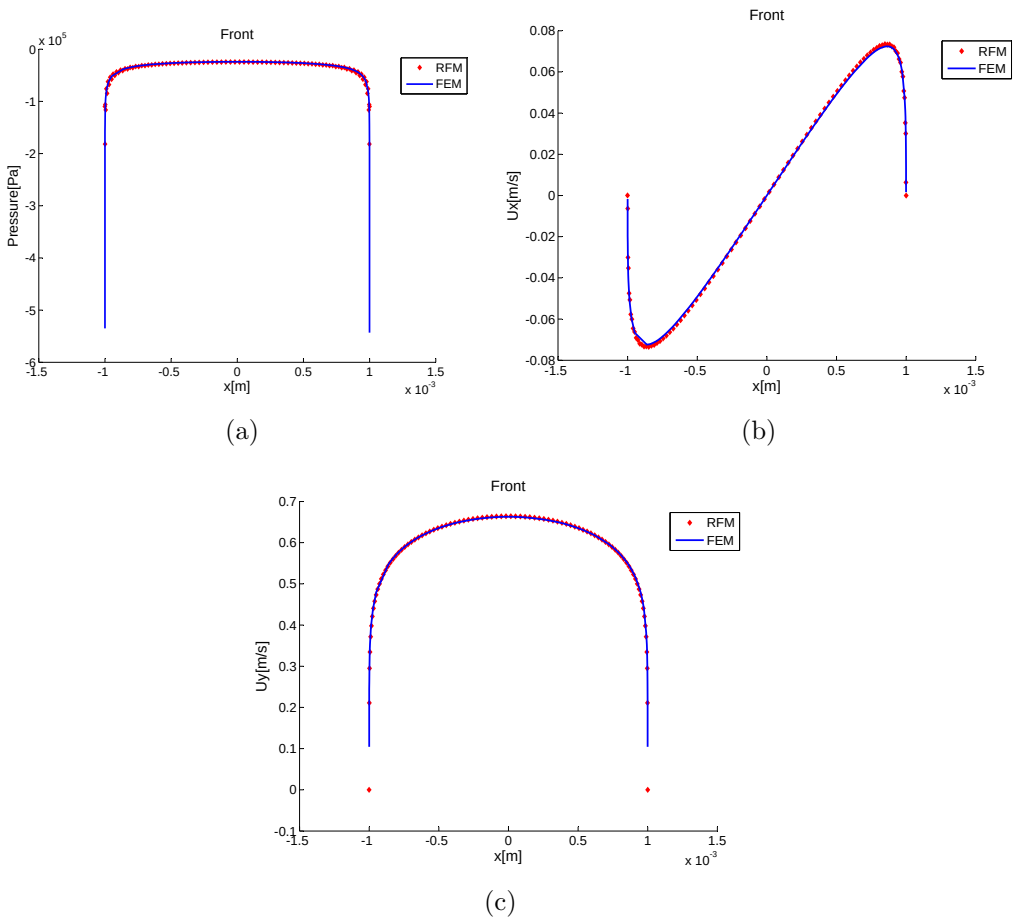

Figure 4.11: Comparison between the pressures and velocities obtained by FEM (COMSOL) and RFM for the flow front and $n = 0.6$.

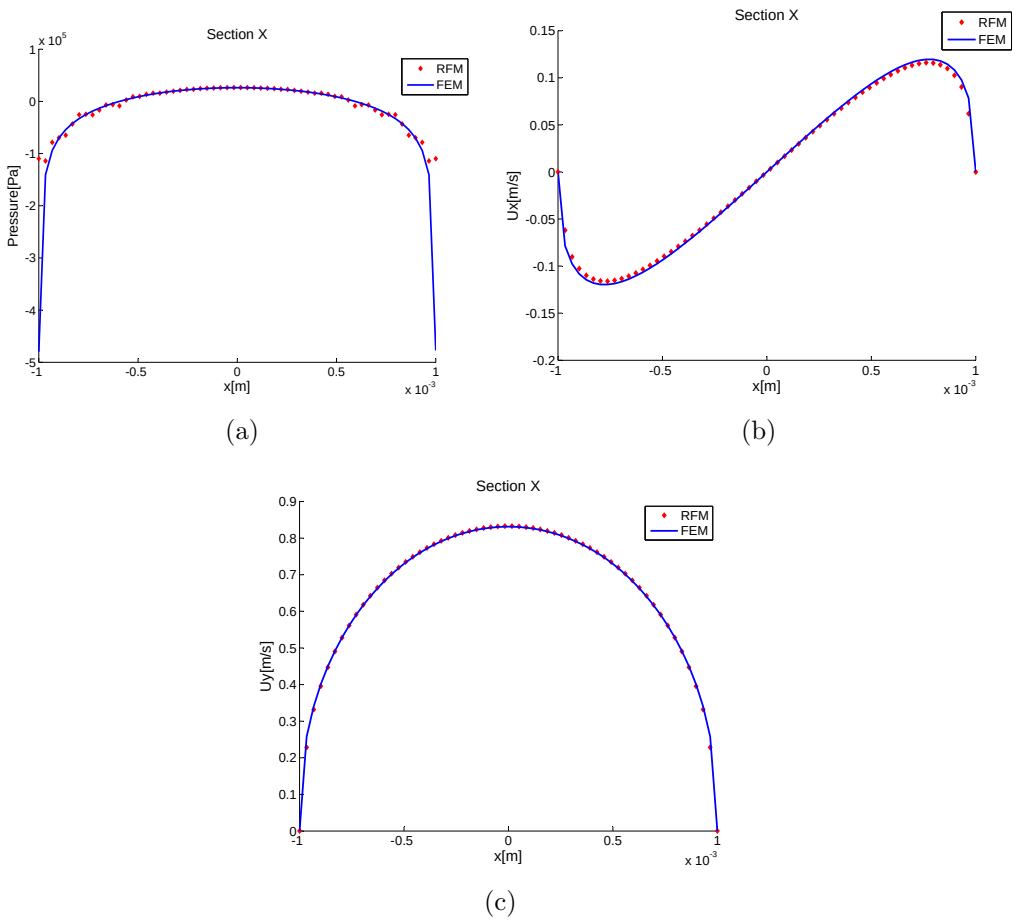

Figure 4.12: Comparison between the pressures and velocities obtained by FEM (COMSOL) and RFM for section X and $n = 0.6$.

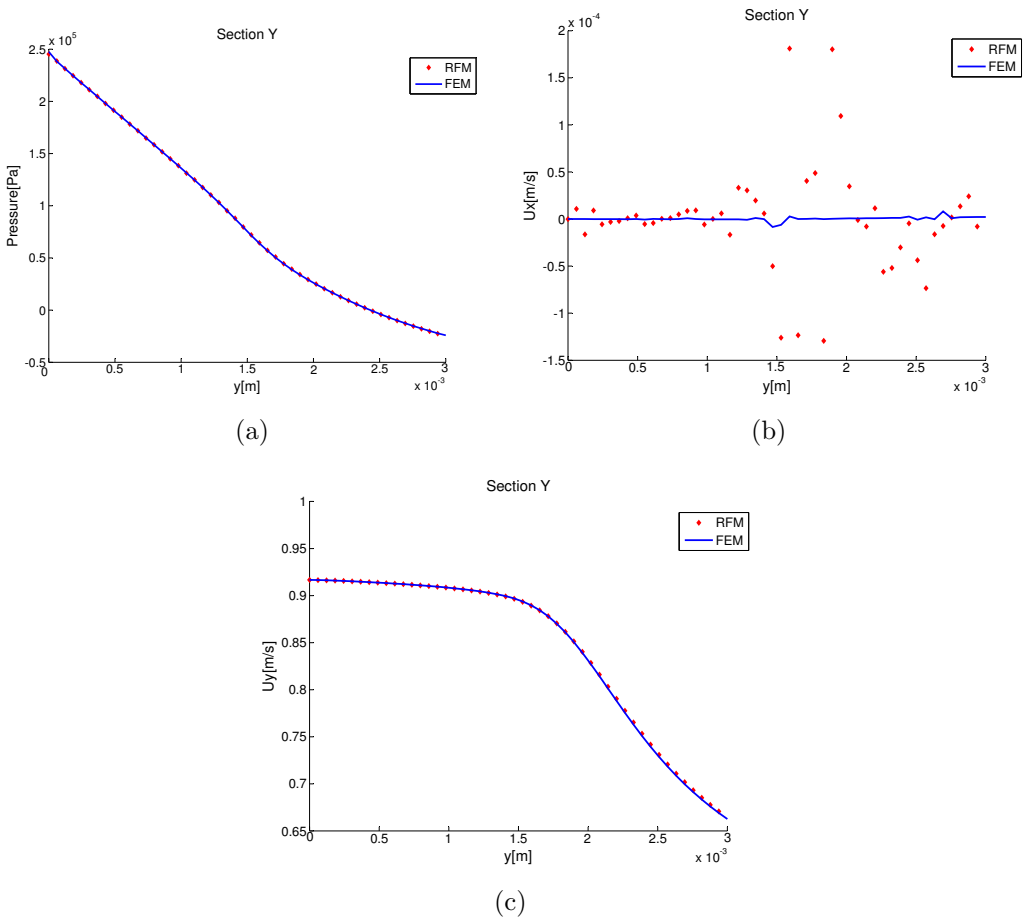

Figure 4.13: Comparison between the pressures and velocities obtained by FEM (COMSOL) and RFM for section Y and $n = 0.6$.

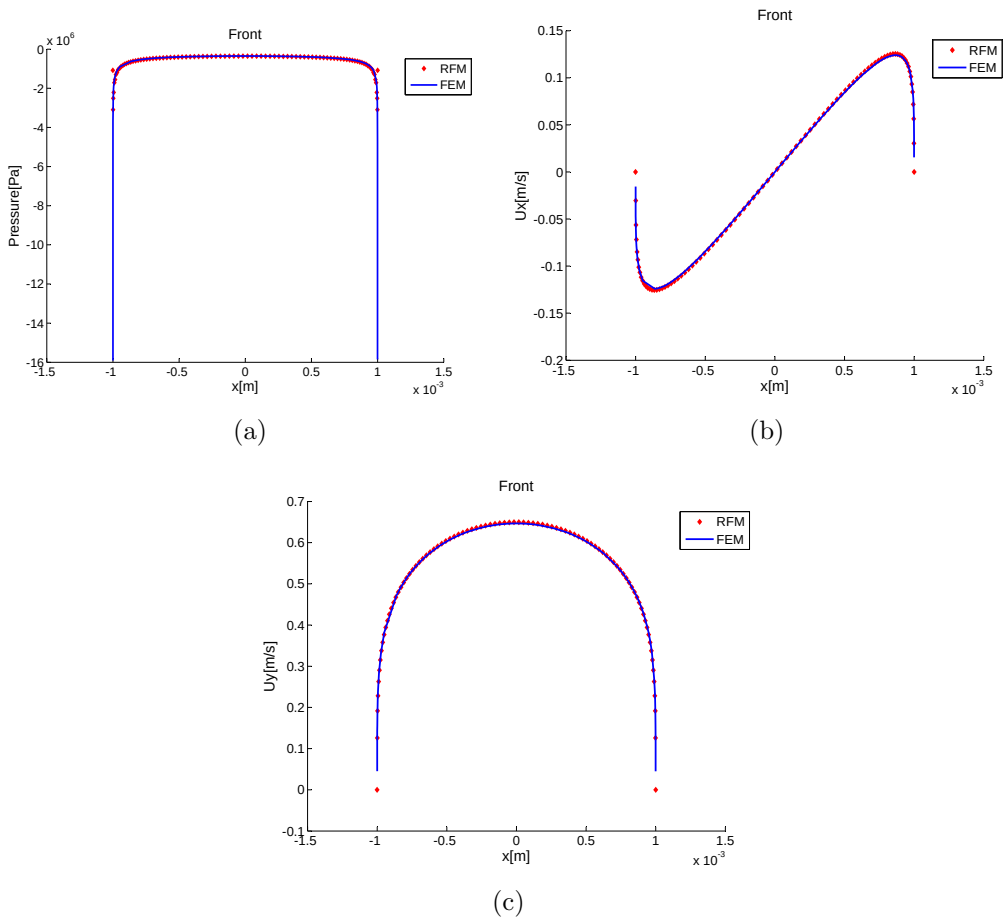

Figure 4.14: Comparison between the pressures and velocities obtained by FEM (COMSOL) and RFM for the flow front and $n = 1$.

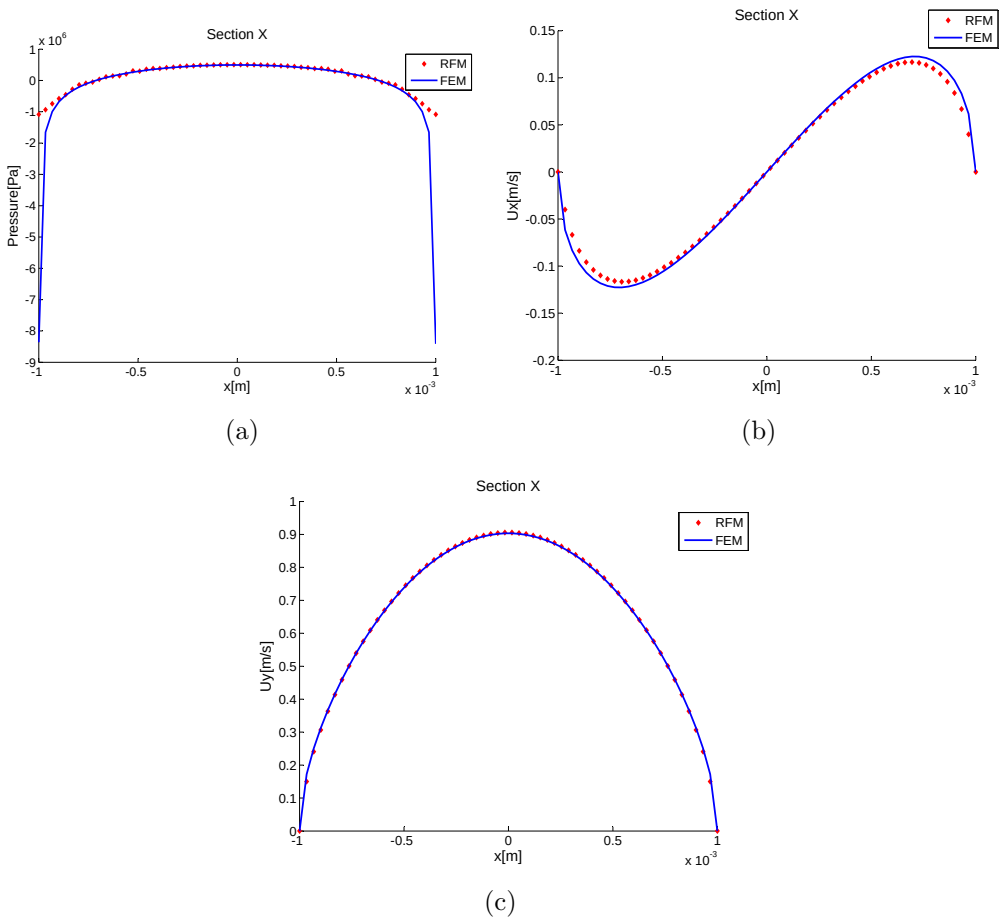

Figure 4.15: Comparison between the pressures and velocities obtained by FEM (COMSOL) and RFM for section X and $n = 1$.

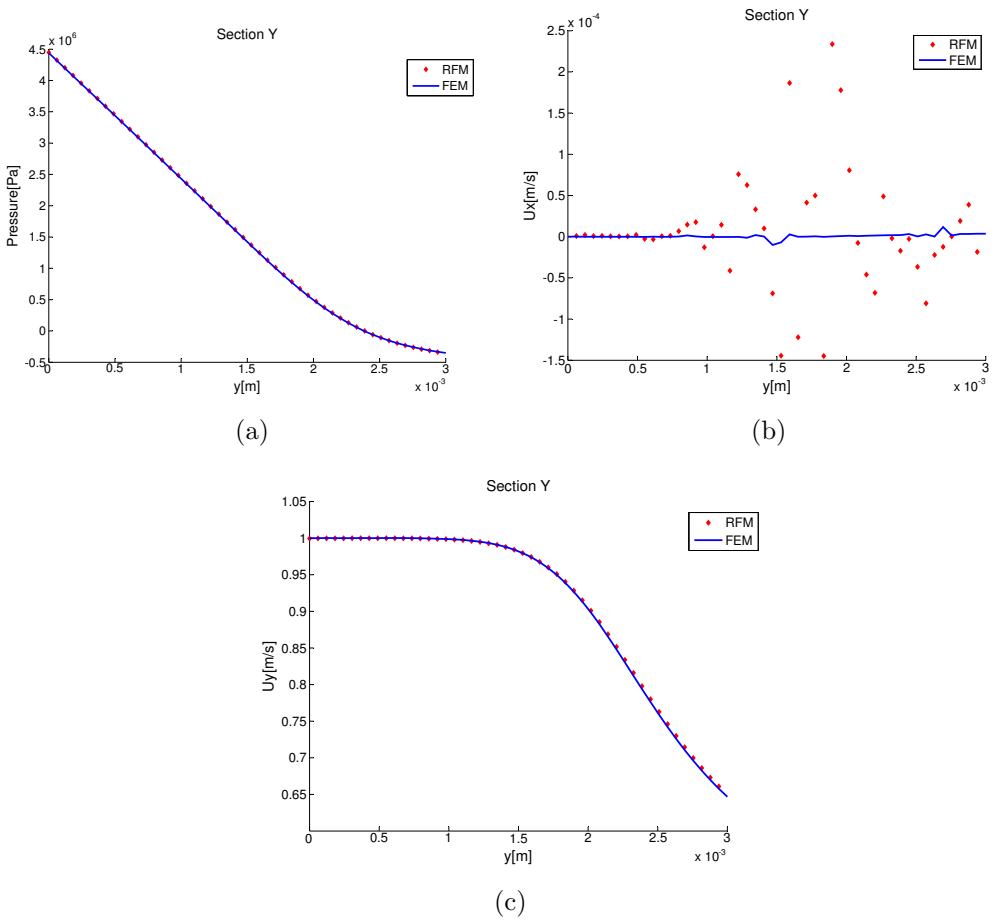

Figure 4.16: Comparison between the pressures and velocities obtained by FEM (COMSOL) and RFM for section Y and $n = 1$.

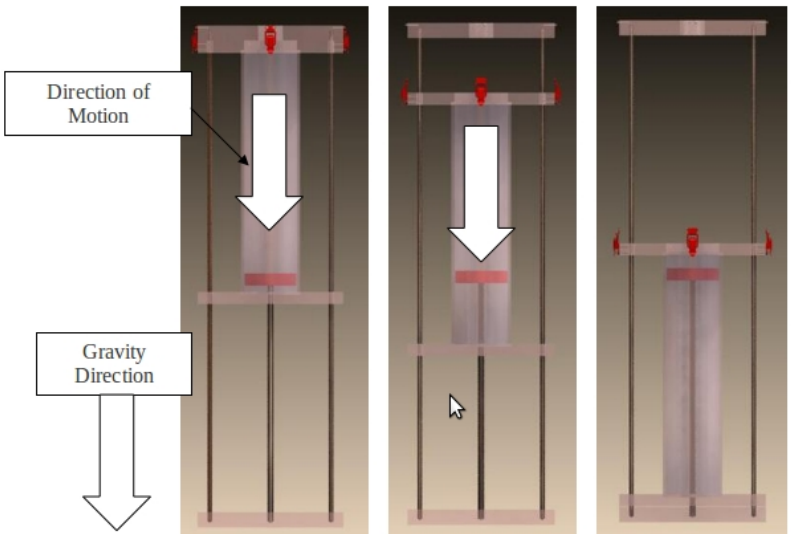

Figure 4.17: Experimental setup designed to study the movement of fibers in a fountain flow velocity field[1].

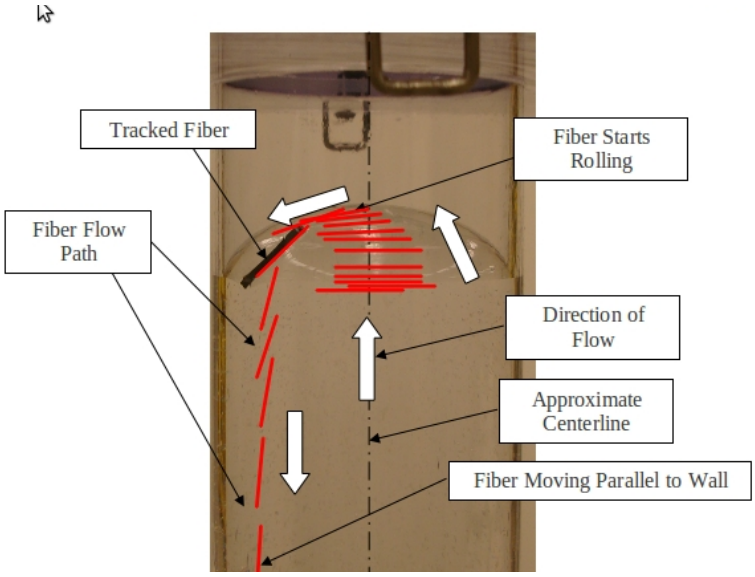

Figure 4.18: Fiber motion in a fountain flow velocity field[1].

$$\frac{\partial u_R}{\partial R} + \frac{u_R}{R} + \frac{\partial u_z}{\partial z} = 0 \tag{4.36}$$

$$0 = -\frac{\partial p}{\partial R} + \mu \left[\frac{\partial^2 u_R}{\partial R^2} + \frac{1}{R}\frac{\partial u_R}{\partial R} - \frac{u_R}{R^2} + \frac{\partial^2 u_R}{\partial z^2} \right] \tag{4.37}$$

$$0 = -\frac{\partial p}{\partial z} + \mu \left[\frac{\partial^2 u_z}{\partial R^2} + \frac{1}{R}\frac{\partial u_z}{\partial R} + \frac{\partial^2 u_z}{\partial z^2} \right] + \rho g_z \tag{4.38}$$

Where the upper case R is used to notate the coordinate in the radius, in order to avoid the confusion with the euclidean distance between the collocation points and the centers which is represented by the lowercase r.

These equations can be expressed in RBF notation (equations 4.39, 4.40, 4.41):

$$\sum_{j=1}^{N} \left[\frac{\partial \phi_u (r_{ij})}{\partial r}\frac{\partial r}{\partial R} + \frac{\phi_u (r_{ij})}{R} \right] \lambda_j + \sum_{j=1}^{N} \left[\frac{\partial \phi_u (r_{ij})}{\partial r}\frac{\partial r}{\partial z} \right] \xi_j = 0 \tag{4.39}$$

$$0 = -\sum_{j=1}^{N_p} \left[\frac{\partial \phi_p (r_{ij})}{\partial r}\frac{\partial r}{\partial R} \right] \beta_j + \sum_{j=1}^{N} \left[\nabla^2 \phi_u (r_{ij}) + \frac{1}{R}\frac{\partial \phi_u (r_{ij})}{\partial r}\frac{\partial r}{\partial R} - \frac{\phi_u (r_{ij})}{R^2} \right] \mu \lambda_j \tag{4.40}$$

$$0 = -\sum_{j=1}^{N_p} \left[\frac{\partial \phi_p (r_{ij})}{\partial r}\frac{\partial r}{\partial z} \right] \beta_j + \sum_{j=1}^{N} \left[\nabla^2 \phi_u (r_{ij}) + \frac{1}{R}\frac{\partial \phi_u (r_{ij})}{\partial r}\frac{\partial r}{\partial R} \right] \mu \xi_j + \rho g_z \tag{4.41}$$

In this particular experimental setup the body forces (gravity) cannot be neglected and remain in the motion equation in z. For this particular set of simulations, the condition of symmetry with respect to the z axis is considered, and is given by equations 4.42, 4.43 and 4.44.

$$u_R = 0 \tag{4.42}$$

$$\frac{\partial u_z}{\partial R} = 0 \tag{4.43}$$

$$\frac{\partial p}{\partial R} = 0 \tag{4.44}$$

These conditions can then be expressed in RFM notation as follows (equations 4.45, 4.46 and 4.47):

$$\sum_{j=1}^{N} \phi_u \left(r_{ij}\right) \lambda_j = 0 \tag{4.45}$$

$$\sum_{j=1}^{N} \frac{\partial \phi_u \left(r_{ij}\right)}{\partial r} \frac{\partial r}{\partial R} \xi_j = 0 \tag{4.46}$$

$$\sum_{j=1}^{N_p} \frac{\partial \phi_p \left(r_{ij}\right)}{\partial r} \frac{\partial r}{\partial R} \beta_j = 0 \tag{4.47}$$

4.3.2 Results

For these simulations, the height of the silicon oil column is assumed to be equal to $3D$, where $D = 95.25mm$ is the diameter of the sleeve. Two simulations were developed: in the first, the entire column is simulated including the non slip condition at the plunger; in the second, the domain has a length of $1.5D$. For the second one, the assumption is that the flow will be completely developed in a length of $1.5D$ and that the plunger does not affect the velocity and pressure fields in the upper part of the column. In the last case, the velocity profile at the entry of the domain is assumed to be parabolic (which is the case in a developed, laminar, pressure flow in a tube). In both cases, the velocity of the wall is equal to $-0.05m/s$ and the viscosity of the oil is taken as $3Pa.s$. The assumption of a developed flow for $z = 1.5D$ was validated as a result of the first simulation and agrees with the observations of other researchers [7]. At the beginning, the front is assumed to be flat, and the final form is obtained via iteration. The results corresponding to the pressure and velocity fields are shown in Figures 4.19, 4.20 and 4.21.

Mitsoulis[28] simulated the fountain flow effect for a Newtonian Fluid in an axisymmetric geometry without gravity obtaining a value of $\chi = 0.84$. Using RFM and including the gravity, the values of χ were 0.67 and 0.64 for the first and second simulations. Therefore, it is concluded that gravity affects the shape of the flow front flattening it, which has been also noticed

by other researchers[7]. Besides, the singularity in the pressure field that could be easily observed in the case of the slit flow without body forces is not so easy to visualize and tends to be less prominent as the body forces tend to be of more importance for the resulting pressure field that the viscous forces. Although the results of these simulations agree qualitatively with the patterns of fiber motions observed experimentally [1], since the velocity was not accurately controlled in the setup of Al-Zain, no quantitative comparison was made between the simulations and the experimental results. Additionally, in the modeling of the problem, the superficial tension and inertia were neglected. This is the standard practice in the modeling of the injection molding process because typically the Reynolds numbers and the inverse of the capillary numbers are very low (several orders of magnitude smaller than one). However, in this particular experimental setup, these two factors could influence the results and should be included in future works.

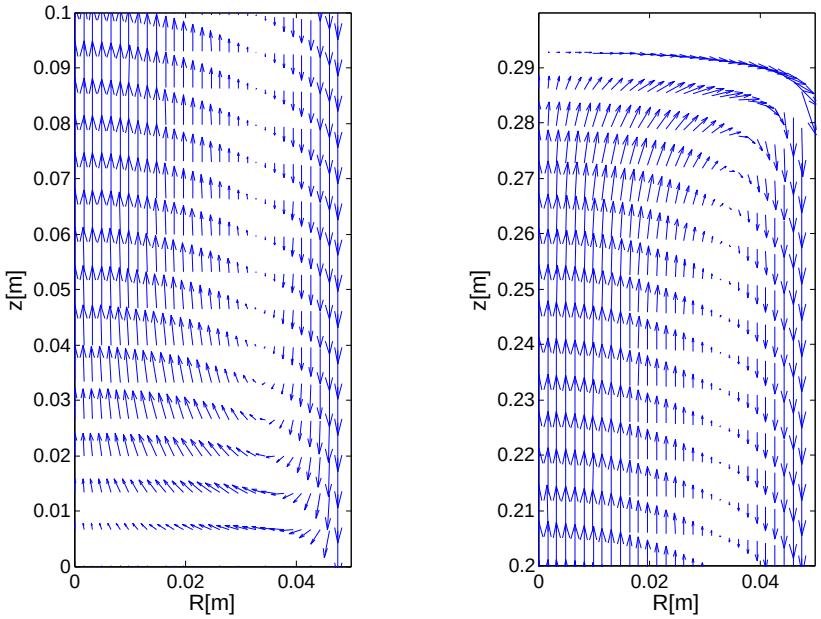

(a) Lower part of the domain

(b) Upper part of the domain

Figure 4.19: Axisymmetric Newtonian case with body forces. Arrow plots of the velocity field (L=3D).

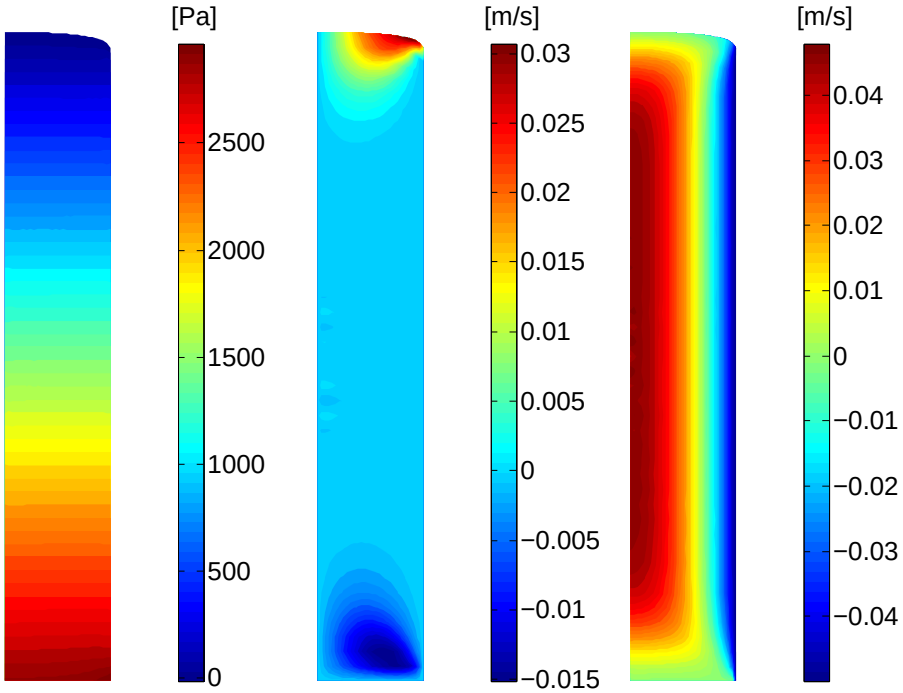

(a) Pressure (b) Velocity in R (c) Velocity in z

Figure 4.20: Axisymmetric Newtonian case with body forces. Velocity and pressure fields (L=3D).

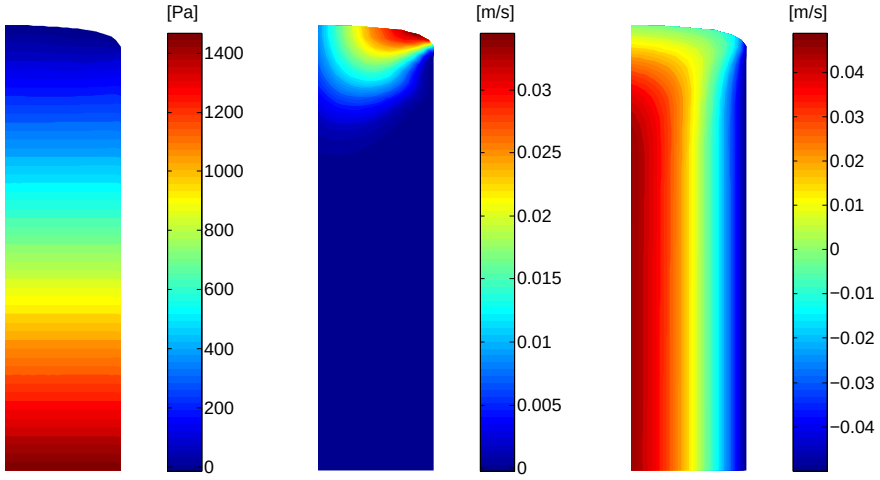

(a) Pressure (b) Velocity in R (c) Velocity in z

Figure 4.21: Axisymmetric Newtonian case with body forces. Velocity and pressure fields (L=1.5D).

4.4 Fountain Flow Effect on Fiber Matrix Separation during Manufacturing of Short Fiber Filled Injection Parts

In 2010, Kurth coupled the results (velocity field corresponding to the Newtonian case) of this thesis with a mechanistic model to simulate the movement of short fibers near the flow front region. The fibers were modeled as beads connected by springs (Figure 4.22). The details of the numerical implementation and results can be found in [17, 16].

For the simulations, initially the fibers were set near the inlet forming a cluster and having a random orientation. Then, the position of these fibers as they moved through the fountain flow region was recorded as shown in Figure 4.23.

In all the simulations of the fiber movements, fiber free regions developed at the mold surface. The reason for this was that fibers tend to interact with each other (friction effects, lubrication effects or mechanical interlock) and due to those interactions, they are restricted from reaching the flow front. Therefore, they tend to stay in the core of the piece.

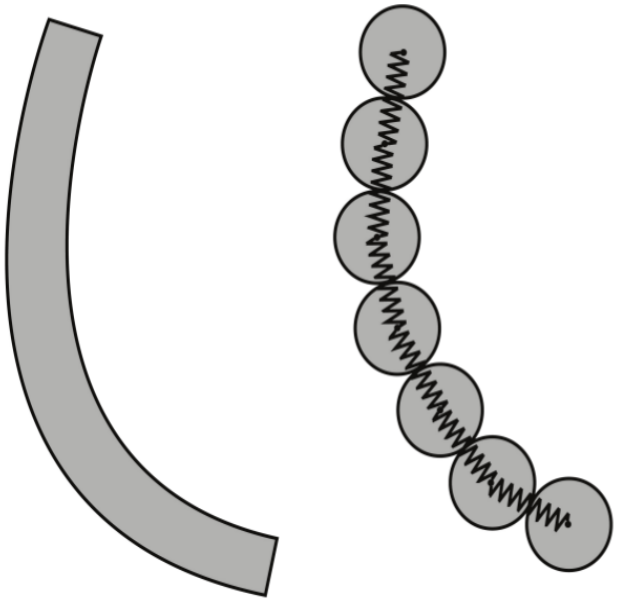

Figure 4.22: Modeling of a single fiber as set of beads connected by springs[16].

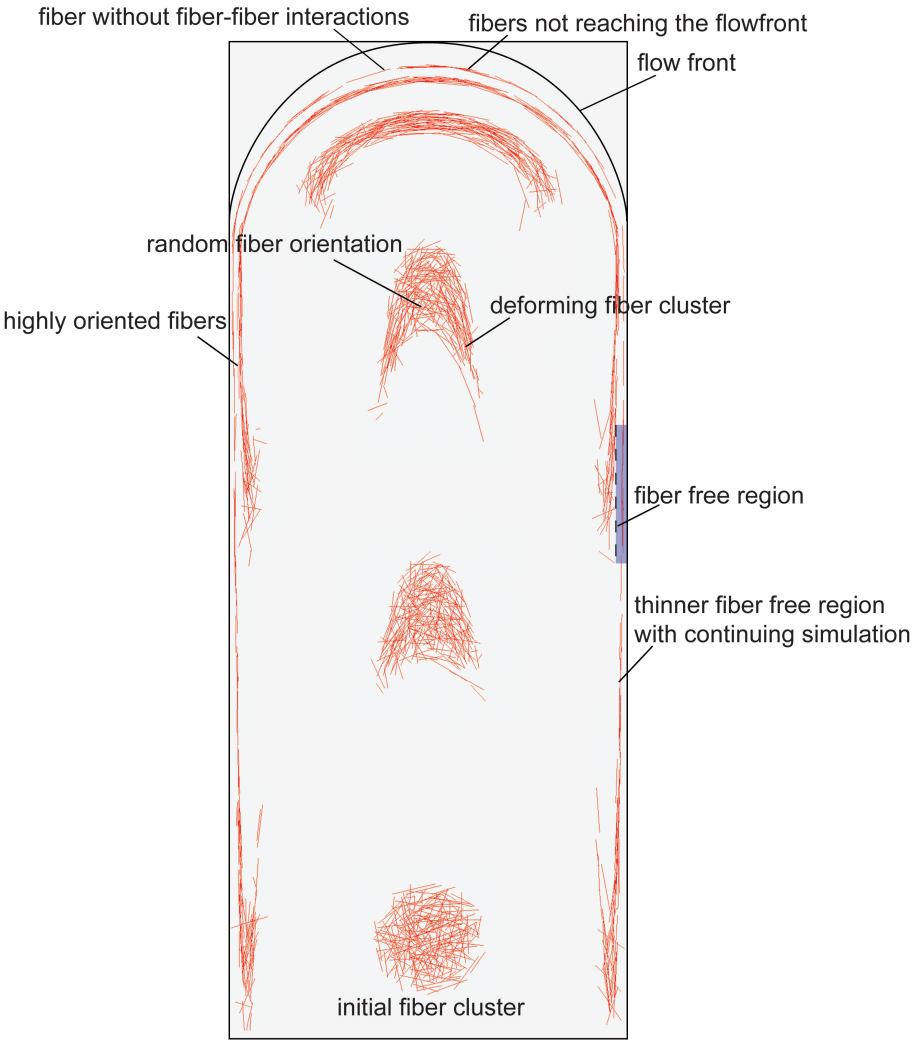

Figure 4.23: Fiber motion in the fountain flow region[16].

Chapter 5

Conclusions

- The fountain flow effect was successfully simulated using the radial functions method for the Newtonian and Power-Law cases. In both cases, the results of the simulations are in good agreement with the literature. To the knowledge of the author, this phenomenon has not been previously simulated by using a meshless technique. For power law parameters in the range of $1.1 \geq n \geq 0.6$, the front flow shape is nearly semicircular and the kinematics of the fountain flow effect are only slightly affected by the shear thinning behavior: the changes in the stream line plots of the velocity field are relatively small.

- In the work of Kurth [17], the data obtained in this thesis has been successfully coupled with mechanistic fiber to simulate the movement of fibers in an injection molding process. The existence of fiber-free regions in the surface of injection molded pieces has been explained as a result of the fiber-fiber interaction in a fountain-flow velocity field.

- Regarding the axis-symmetric case with gravity, the body forces affect the form of the flow front flattening it. Besides, the singularity in the pressure field tends to be less noticeable and is masked by the influence of gravity in the pressure field.

Chapter 6

Future Work

In order to adequately asses the importance of the fountain flow effect in injection molding, non-steady simulations including the filling of complete pieces should be developed. As has already been mentioned in the conclusions, the data of this work has been used in collaboration with other researchers to explain the phenomenon of fiber matrix separation in injection molded parts. In order to continue with this line of work, the formation of the skin due to the solidification of the polymer as it contacts the wall should be included in the simulations.

In this work, only the power law model with relatively high values of n was used to describe the variation of viscosity with the shear rate. In future works, the inclusion of models capable of describing the viscoelastic behavior of polymers should be implemented.

In the case of the mock-up setup designed to study the motion of fibers in the fountain flow velocity field (axisymmetric case with body forces), future works should include the superficial tension and the inertia terms of the equation of motion in the simulations.

Bibliography

[1] H. Al-Zain. *Effect of Fountain Flow on Fiber-Matrix Separation in Fiber Reinforced Injection Molded Parts*. PhD thesis, University of Wisconsin Madison, 2010.

[2] D. Baird and D. Collias. *Polymer Processing: Principles and Design*. John Wiley & Sons, INC, United States of America, 1st edition, 1998.

[3] R. A. Behrens, M. J. Crochet, C. D. Denson, and A. B. Metzner. Transient free-surface flows: motion of a fluid advancing in a tube. *AIChE Journal*, 33(7):1178–1186, 1987.

[4] A. N. Beris. Fluid elements deformation behind an advancing flow front. *Journal of Rheology*, 31(2):121–124, 1987.

[5] A. C. B. Bogaerds, M. A. Hulsen, G. W. M. Peters, and F. P. T. Baaijens. Stability analysis of injection molding flows. *Journal of Rheology*, 48(4):765–785, 2004.

[6] C. S. Chen, M. A. Goldberg, and R. S. Schaback. *Recent developments of the dual reciprocity method using compactly supported radial basis functions*. WIT Press, Southampton, Boston, 2003.

[7] D. J. Coyle, J. W. Blake, and C. W. Macosko. The kinematics of fountain flow in mold filling. *AIChE Journal*, 33(7):1168–1177, 1987.

[8] O. Estrada. Desarrollo de un modelo computacional basado en funciones de base radial para la simulación en 2d del flujo no isotérmico de polímeros a través de un cabezal para perfilería. Master's thesis, Universidad EAFIT, 2005.

[9] M. J. García. *The Finite Element Method, in Lectures Notes on Numerical Analysis*. Fondo Editorial Universidad EAFIT, Medellín, 2008.

[10] H. Gramberg, J. van Vroonhoven, and A. van de Ven. Flow patterns behind the free flow front for a Newtonian fluid injected between two infinite parallel plates. *European Journal of Mechanics - B/Fluids*, 23(4):571–585, 2004.

[11] H. J. J. Gramberg. *Flow Front Instabilities in an Injection Moulding Process*. PhD dissertation, Technische Universiteit Eindhoven, 2005.

[12] R. Huilgol and Z. You. On the importance of the pressure dependence of viscosity in steady non-isothermal shearing flows of compressible and incompressible fluids and in the isothermal fountain flow. *Journal of Non-Newtonian Fluid Mechanics*, 136(2-3):106–117, 2006.

[13] M. R. Kamal and V. Tan. Orientation in injection molded polystyrene. *Polymer Engineering and Science*, 19(8):558–563, 1979.

[14] A. Karageorghis, C. Chen, and Y.-S. Smyrlis. A matrix decomposition rbf algorithm: Approximation of functions and their derivatives. *Applied Numerical Mathematics*, 57:304–319, 2007.

[15] R. E. Khayat, A. Derdouri, and L. Hebert. A three-dimensional boundary-element approach to gas-assisted injection molding fluids and in the isothermal fountain flow. *Journal of Non-Newtonian Fluid Mechanics*, 57(2-3):253–270, 1995.

[16] K. Kurth. Simulation of fiber motion within the fountain flow region during injection molding. Master's thesis, University of Wisconsin Madison, 2010.

[17] K. H. Kurth, D. Ramírez, I. López, N. Rudolph, and T. A. Osswald. Fiber motion in fountain flow and its relation to fiber free regions at the surface of injection molded parts. In *ANTEC*, Boston, MA, 2011. SPE(Society of Plastics Engineers).

[18] E. Larsson and B. Fornberg. A numerical study of some radial basis function based solution methods for elliptic PDEs. *Computers and Mathematics with Applications*, 46:891–902, 2003.

[19] S.-L. Lee and W.-C. Liao. Numerical simulation of a fountain flow on nonstaggered cartesian grid system. *International Journal of Heat and Mass Transfer*, 51(9-10):2433–2443, 2008.

[20] J. Li, A. Cheng, and C.-S. Chen. A comparison of efficiency and error convergence of multiquadric collocation method and finite element method. *Engineering Analysis with Boundary Elements*, 27(3):251–257, 2003.

[21] I. D. López. *Modeling of polymer processing using the radial function method (RFM).* PhD thesis, University of Wisconsin Madison, 2009.

[22] H. Mavridis, A. Hrymak, and J. Vlachopoulos. Deformation and orientation of fluid elements behind an advancing front. *Journal of Rheology*, 30(6):555–563, 1986.

[23] H. Mavridis, A. Hrymak, and J. Vlachopoulos. The effect of fountain flow on molecular orientation in injection molding. *Journal of Rheology*, 32:639–663, 1988.

[24] H. Mavridis, A. N. Hrymak, and J. Vlachopoulos. Finite element simulation of fountain flow in injection molding. *Polymer Engineering and Science*, 26(7):449–454, 1986.

[25] H. Mavridis, A. N. Hrymak, and J. Vlachopoulos. Transient free-surface flows in injection molding. *AIChE Journal*, 34(3):403–410, 1988.

[26] S. Middleman. *Fundamentals of Polymer Processing.* McGraw-Hill College, 1977.

[27] E. Mitsoulis. Effect of viscoelasticity in fountain flow of polyethylene melts. *International Polymer Processing*, 5:439–451, 2009.

[28] E. Mitsoulis. Fountain flow of pseudoplastic and viscoplastic fluids. *Journal of Non-Newtonian Fluid Mechanics*, 165:45–55, 2010.

[29] E. Mitsoulis. Fountain flow revisited: The effect of various fluid mechanics parameters. *AIChE Journal*, 56(5):1147–1162, 2010.

[30] T. Osswald and J. P. Hernández. *Polymer Processing, Modeling and Simulation.* Hanser Gardner Publications, München, Germany, 1st edition, 2006.

[31] T. Osswald and G. Menges. *Materials Science of Polymers for Engineers.* Hanser Gardner Publications, Munich, Germany, 2nd edition, 2003.

[32] T. Osswald, L.-S. T. Turng, and P. Gramann. *Injection Molding Handbook*. Hanser, Munich, 1st edition, 2002.

[33] H. Power and V. Barraco. Comparison analysis between unsymmetric and symmetric radial basis function collocation methods for the numerical solution of partial differential equations. *Computer and Mathematics with Applications*, 43:551–583, 2002.

[34] D. Ramírez, W. Ospina, M. García, and O. Estrada. Comparación entre los métodos colocación con funciones de base radial (RBFCM) y elementos finitos(FEM) para la solución de la ecuación de Poisson. In *VII Congreso Colombiano de Modelamiento Numérico*, 2009.

[35] W. Rose. Fluid-fluid interfaces in steady motion. *Nature*, 191:242–243, 1961.

[36] T. Sato and S. M. Richardson. Numerical simulation of the fountain flow problem for viscoelastic liquids. *Polymer Engineering and Science*, 35:805–812, 1995.

[37] Y. K. Shen. Study on moving boundary problems of injection molding. *International Communications in Heat and Mass Transfer*, 25(5):701–710, 1998.

[38] J. R. Shewchuk. Triangle: Engineering a 2D Quality Mesh Generator and Delaunay Triangulator. In M. C. Lin and D. Manocha, editors, *Applied Computational Geometry: Towards Geometric Engineering*, volume 1148 of *Lecture Notes in Computer Science*, pages 203–222. Springer-Verlag, May 1996. From the First ACM Workshop on Applied Computational Geometry.

[39] Z. Tadmor and C. G. Gogos. *Principles of Polymer Processing*. John Wiley & Sons, United States of America, 2nd edition, 2006.

[40] J. C. W. van Vroonhoven and W. J. J. Kuijpers. A free boundary problem for viscous fluid flow in injection molding. *Journal of Engineering Mathematics*, 24(2):151–165, 1990.

[41] J. Vlachopoulos. An overview of polymer processing. *Materials Science and Technology*, 19(9):1161–1169, 2003.